The Astrophysical Journal, 1003:98 (19pp), 2026 May 20 https://doi.org/10.3847/1538-4357/ae64f0

The Supermassive Black Hole in the Nearby Spiral Galaxy M81: A Robust Mass from JWST/NIRSpec Stellar Dynamics

Dieu D. Nguyen[1], Tuan N. Le[2], Michele Cappellari[3], Hai N. Ngo[2], Tinh Q. T. Le[4], Tien H. T. Ho[2], Long Q. T. Nguyen[2], Elena Gallo[1], Fan Zou[1], Michele Perna[5], Niranjan Thatte[3], and Miguel Pereira-Santaella[6]
[1] Department of Astronomy, University of Michigan, 1085 South University Avenue, Ann Arbor, MI 48109, USA; dieun@umich.edu
[2] Faculty of Physics–Engineering Physics, University of Science, Vietnam National University, Ho Chi Minh City, Vietnam
[3] Subdepartment of Astrophysics, Department of Physics, University of Oxford, Denys Wilkinson Building, Keble Road, Oxford OX1 3RH, UK
[4] Department of Physics, International University, Vietnam National University, Ho Chi Minh City, Vietnam
[5] Centro de Astrobiología (CAB), CSIC–INTA, Departamento de Astrofísica, Calle Ajalvir Kilometer 4, 28850 Torrejón de Ardoz, Madrid, Spain
[6] Instituto de Física Fundamental, CSIC, Calle Serrano 123, 28006 Madrid, Spain
Received 2026 January 23; revised 2026 April 20; accepted 2026 April 23; published 2026 May 19

Abstract

Despite its proximity, the mass of the supermassive black hole (SMBH) in the spiral galaxy M81 (NGC 3031) has remained a subject of discussion, with doubts previously cast on the reliability of available dynamical measurements. We present the first robust stellar-dynamics measurement of its mass using high-resolution, two-dimensional kinematics from JWST/NIRSpec observations of the central $3'' \times 3''$. By tracing stellar motions in the near-infrared, our data penetrate the obscuring nuclear dust and allow for the separation of stellar light from the nonthermal AGN continuum. We modeled the kinematics using the Jeans anisotropic modelling method. Rather than relying on a standard Bayesian approach for error estimation, we constructed a suite of 24 independent models, each employing a unique combination of different physical assumptions regarding stellar mass-to-light (M/L) ratio gradients, the point-spread function, the masking of the central active galactic nucleus, and the orientation of the velocity ellipsoid. This ensemble approach allows us to robustly account for the impact of systematic uncertainties. To estimate our systematic uncertainties, we performed a bootstrap of the $M_{\rm BH}$ values derived from these 24 models, thereby incorporating the variance between different physical assumptions. Our analysis yields a precise SMBH mass of $M_{\rm BH} = (4.77 \pm 0.37) \times 10^7\, M_\odot$ (1σ confidence, including systematic and statistical uncertainties). This result is consistent with previous determinations within their uncertainties, while providing a crucial and highly reliable anchor point for SMBH–galaxy scaling relations in spiral galaxies.

Unified Astronomy Thesaurus concepts: Astrophysical black holes (98); Galaxy dynamics (591); Galaxy kinematics (602); Galaxy nuclei (609); Galaxy spectroscopy (2171); Astronomy data modeling (1859)

Materials only available in the online version of record: machine-readable table

1. Introduction

The masses of supermassive black holes (SMBHs; $M_{\rm BH} \approx 10^{6-10}\, M_\odot$) are known to correlate tightly with the global properties of their host galaxies, establishing a fundamental link between their evolution. These scaling relations, such as the $M_{\rm BH}$–σ relation, have been established and refined in numerous studies (e.g., K. Gültekin et al. 2009; N. J. McConnell & C.-P. Ma 2013; R. P. Saglia et al. 2016; R. C. E. van den Bosch 2016), and are comprehensively reviewed in J. Kormendy & L. C. Ho (2013). Accurately measuring $M_{\rm BH}$ is crucial for calibrating these scaling relations, but it remains a significant observational challenge. The most reliable measurements are derived from dynamical modeling of the gravitational potential, using the motions of various tracers. These include stars (e.g., E. K. Verolme et al. 2002; K. Gebhardt et al. 2003; M. Cappellari et al. 2009; D. D. Nguyen et al. 2014, 2017, 2018, 2019; J. L. Walsh et al. 2016; D. D. Nguyen 2017; C. P. Ahn et al. 2018; D. Krajnović et al. 2018; K. T. Voggel et al. 2018; S. Thater et al. 2019, 2022, 2023), ionized gas (e.g., A. J. Barth et al. 2001; K. L. Shapiro et al. 2006; N. Neumayer et al. 2007), and molecular gas (e.g., T. A. Davis et al. 2013; K. Onishi et al. 2017; D. D. Nguyen 2019; T. A. Davis et al. 2020; D. D. Nguyen et al. 2020, 2021, 2022; H. N. Ngo et al. 2025b).

The nearby spiral galaxy M81 (NGC 3031) is a prime example of the difficulties in measuring black hole (BH) masses. Throughout this paper, we adopt a distance of $D = 3.63 \pm 0.14$ Mpc (P. R. Durrell et al. 2010). This value represents the mean of five independent determinations: one based on Cepheid variables (W. L. Freedman et al. 1994; L. Ferrarese et al. 2000; L. P. McCommas et al. 2009) and four derived from the tip of the red giant branch (TRGB) method (N. A. Tikhonov & O. A. Galazutdinova 2005; L. Rizzi et al. 2007; J. J. Dalcanton et al. 2009; P. R. Durrell et al. 2010).

Despite its proximity, a definitive measurement of the SMBH mass in M81 has remained elusive. To date, two direct dynamical modeling determinations have been attempted, although doubts regarding their reliability have been raised in the literature (e.g., see discussion in the box at pg. 552 of the review by e.g., J. Kormendy & L. C. Ho 2013). The first was a preliminary stellar-dynamics measurement based on a two-integral Jeans model of long-slit Hubble Space Telescope (HST)/Space Telescope Imaging Spectrograph (STIS) observations (G. A. Bower et al. 2000), yielding $M_{\rm BH} = (6 \pm 20\%) \times 10^7\, M_\odot$. This initial value was presented in an AAS Bulletin abstract and was not finalized in a peer-reviewed paper. The second determination utilized ionized gas

kinematics to estimate $M_{\rm BH} = (7 \pm 2) \times 10^7\ M_\odot$ (N. Devereux et al. 2003). While methodological caveats for both studies were highlighted by J. Kormendy & L. C. Ho (2013), it is notable that our new independent measurement is consistent with these earlier determinations within their reported uncertainties. Our study provides a precision measurement that confirms the scale of the BH mass suggested by these previous works while significantly reducing the statistical and systematic uncertainties. The historical difficulty of this measurement is further compounded by the presence of a low-luminosity active galactic nucleus (LLAGN; M. Eracleous et al. 2010) and complex dust structures associated with both inflows (A. Schnorr Müller et al. 2011) and outflows (F. Shi et al. 2021), which can bias observations made at optical wavelengths (S. Thater 2019).

The advent of the James Webb Space Telescope (JWST) offers a transformative opportunity to overcome these challenges. By targeting the CO band head absorption features in the near-infrared (NIR) at $\sim$2.3 μm, the NIRSpec instrument can trace stellar motions directly, penetrating the obscuring dust that affects optical studies (e.g., M. Cappellari et al. 2009). Adopting a velocity dispersion of $\sigma = 162$ km s^{-1} (A. Schnorr Müller et al. 2011) the $M_{\rm BH}$–σ relation by K. Gültekin et al. (2009) predicts an $M_{\rm BH} \approx 5 \times 10^7\ M_\odot$. Given this mass, the SMBH's sphere of influence (SOI) is $r_{\rm SOI} \approx 0\farcs5$. This is more than 3 times the NIRSpec point-spread function (PSF) FWHM at this wavelength (F. D'Eugenio et al. 2024, 2026), ensuring the gravitational influence of the BH is well resolved. These capabilities are crucial for probing the demographic of intermediate-mass BHs ($M_{\rm BH} \approx 10^{2-5}\ M_\odot$) and bona fide massive BHs ($M_{\rm BH} > 1.8 \times 10^7\ M_\odot$; G. Sasseville et al. 2024), a regime that will be further explored by next-generation facilities like the 39 m Extremely Large Telescope (e.g., D. D. Nguyen et al. 2023, 2025a; N. A. Thatte et al. 2024; H. N. Ngo et al. 2025a, 2025).

In this work, we measure the stellar-based SMBH mass in M81 using Jeans anisotropic models (JAMs; M. Cappellari 2008, 2020) applied to archival JWST/NIRSpec G235H/F170LP integral field unit (IFU) data (Program ID (PID): 02016, PI: Anil C. Seth), HST/Wide Field Camera 3 (WFC3) infrared (IR) F110W-band imaging (PID: 11421, PI: H. A. Bushouse), and the J-band image from the Two Micron All Sky Survey (2MASS; T. H. Jarrett et al. 2003). The modeling also constrains key dynamical parameters, including anisotropy, the stellar mass-to-light ratio (M/L_J), and assesses their impact on the inferred $M_{\rm BH}$ (e.g., D. D. Nguyen et al. 2018, 2019) in M81.

It is important to note that the nucleus of M81 exhibits dust structures associated with both inflows (A. Schnorr Müller et al. 2011) and outflows (F. Shi et al. 2021), which can bias optical gas-dynamics measurements (S. Thater 2019). The NIRSpec G235H/F170LP observations mitigate these effects by targeting the CO band head absorption lines (e.g., M. Cappellari et al. 2009) in the NIR, where dust extinction is minimal and stellar motions are traced directly. Thus, our measurements not only refine the $M_{\rm BH}$ estimate for M81, but also demonstrate the remarkable capability of JWST/NIRSpec to probe SMBH demographics.

This paper is organized as follows. In Section 2, we describe the NIRSpec IFU observations, the data reduction, the correction of spectral wiggles in the central regions, and the extraction of the two-dimensional (2D) line-of-sight velocity distribution (LOSVD) from the CO band head features. Section 3 details the construction of the stellar photometric model from the HST F110W- and 2MASS J-band images. In Section 4, we combine the 2D LOSVD and photometric model as input for JAMs to derive $M_{\rm BH}$. Finally, our results and conclusions are presented in Sections 5 and 6, respectively.

2. JWST/NIRSpec Observations and Kinematics

2.1. G235H/F170LP Integral Field Unit Data

M81 was observed on 2022 November 25 with the JWST/NIRSpec IFU using the high spectral resolution grating (G235H/F170LP; $R \sim 2700$), covering the wavelength range between 1.66 and 3.17 μm and a spectral sampling of 4 Å per spectral pixel. This observation employed the NRSIRS2RAPID readout pattern with 14 groups per integration and one integration per exposure, with an effective integration time of 204 s and a total effective exposure time of 1634 s. A four-point medium-cycling dither pattern was used to optimize spatial sampling. The raw data were processed using the JWST calibration pipeline, specifically STScI pipeline version 1.14.0 (H. Bushouse et al. 2024) with the Calibration Reference Data System context `jwst_1242.pmap`.[7] The final data cube was resampled at a pixel scale of 0$\farcs$1, approximately 5 times smaller than the SMBH's $r_{\rm SOI}$ (as discussed in Section 1), and covers the central field of view (FOV) of $3'' \times 3''$.

2.2. Wiggles Corrections

Undersampling of the NIRSpec PSF introduces sinusoidal artifacts, commonly referred to as "wiggles," into individual spaxel spectra of bright sources. These features are largely mitigated when spectra are integrated over apertures of approximately 0$\farcs$2–0$\farcs$5 (D. R. Law et al. 2023). Because the standard NIRSpec pipeline does not provide a built-in correction for these artifacts, we employed the empirical routine developed by M. Perna et al. (2023).[8] The method is briefly summarized below.

First, we extracted the spectrum from the brightest spaxel, where wiggles are most prominent, and masked intrinsic emission lines, absorption features, and the spectral gap between the two NIRSpec detectors. We then fit a sinusoidal model within rolling wavelength windows iteratively, allowing the fit to adapt locally to wavelength-dependent variations in wiggle characteristics as shown in Figure 1. This model was calibrated against the spectrum extracted from a 4 pixel radius (0$\farcs$4) circular aperture, centered on the peak of the white-light image, where wiggles are effectively smoothed out. We found that this aperture is sufficient to suppress wiggles in the NIRSpec integral field spectroscopy (IFS) data cube of M81. Finally, the resulting wiggle frequency was adopted as a prior when subtracting the oscillations from all other affected spaxels.

To quantitatively assess the effectiveness of the wiggle correction, we compare the rms of the residuals between the corrected single-spaxel spectrum and the integrated spectrum to the 3σ error envelope, as shown in the bottom panel of Figure 1. Across the full spectral fitting window, the residuals remain within the 1σ noise level, with an rms of $\lesssim$3% of the continuum signal, confirming that the residual wiggles are negligible for the subsequent kinematic analysis. We further

[7] https://jwst-crds.stsci.edu
[8] https://github.com/micheleperna/JWST-NIRSpec_wiggles

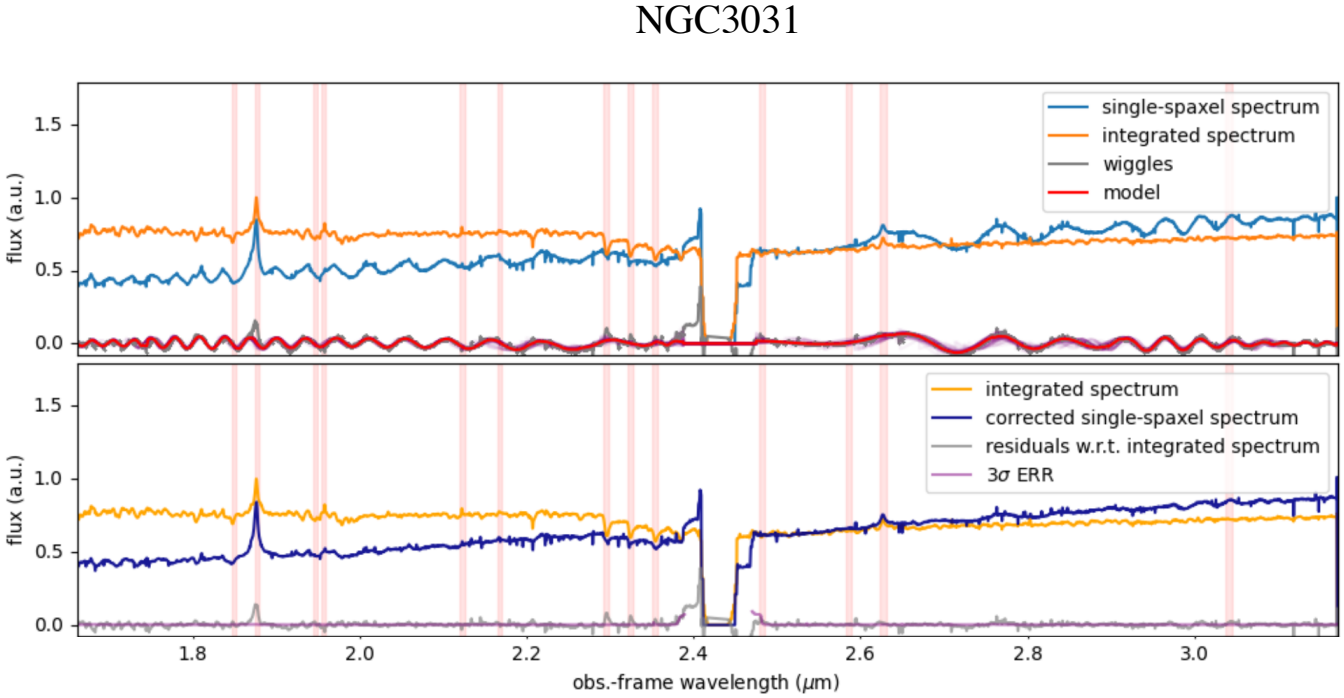

Figure 1. Modeling of wiggles in the single-spaxel NIRSpec spectrum of M81. Top panel: integrated spectrum (orange), single-spaxel spectrum (blue), and residual wiggles (gray). The red curve shows the best-fitting wiggle model. Bottom panel: wiggle-corrected single-spaxel spectrum (dark blue) compared to the integrated spectrum (orange); residuals with respect to the integrated spectrum (gray); and the 3σ uncertainty (purple–pink) after the wiggle correction. In all panels, red shaded regions mark emission lines excluded from the fit.

verified this quantitatively using the reduced χ^2 of the Penalized Pixel-Fitting (PPXF) fit[9] (M. Cappellari & E. Emsellem 2004; M. Cappellari 2017; see Section 2.6), computed for the innermost spaxels within $r_{\rm SOI} \approx 0\farcs5$, where the BH signal is most sensitive, finding $\chi^2_{\rm red} \approx$ 1.5–2.7. We note that the innermost spaxels are subject to additional complexity arising from active galactic nucleus (AGN) continuum contamination; however, this is explicitly accounted for through an ∼15% uncertainty on the central bin kinematics propagated into our dynamical modeling (see Section 2.6), ensuring that our $M_{\rm BH}$ determination remains robust. For a well-constrained PPXF fit with a good signal-to-noise ratio (S/N) in the outer spaxels, we find $\chi^2_{\rm red} \approx$ 1.0–1.5.

All subsequent analyses were performed using the wiggle-corrected data cube.

2.3. Defining the Galaxy Center

Because the kinematic center is less precisely constrained due to its reliance on LOSVD extractions (Section 2.7), we adopted the more accurate photometric center, defined as the weighted barycenter under the assumption that the BH coincides with the surface-brightness peak. To determine the weighted barycenter of the nucleus, we performed a two-step experiment. We first computed the barycenter using the 100 brightest pixels within a $1'' \times 1''$ aperture, then refined the estimate using the 25 brightest pixels within a smaller $0\farcs5 \times 0\farcs5$ region. The two centers agree to within half a pixel ($\Delta x < 0\farcs006$ and $\Delta y < 0\farcs007$), a difference that is too small and unresolvable at the spatial resolution of the NIRSpec IFU data. We therefore adopt the barycenter derived from the larger aperture, as it is constrained by a greater number of spaxels and thus provides a more statistically robust estimate. This photometric, AGN-aligned center was used as the origin in all models and figures.

2.4. Stellar Kinematics Templates and PPXF Setup

As the nucleus of M81 is classified as an LLAGN (M. Eracleous et al. 2010), its nuclear spectra likely contain a substantial contribution from AGN continuum emission in several central spaxels (see Section 2.2). This continuum emission dilutes the stellar CO band head absorption features used to trace stellar kinematics, resulting in underestimated velocity dispersions and reduced line strength (γ; see Section 2.2 of R. P. van der Marel & M. Franx 1993). Additionally, a rising continuum can mimic changes in the stellar population, biasing the template mix and further reducing the reliability of the velocity-dispersion measurement.

Following M. Cappellari et al. (2009), D. A. Simon et al. (2024), and D. D. Nguyen et al. (2026), we defined the observed line strength as γ = stars/(stars + AGN), representing the fraction of flux attributed to the stellar template within the fitted spectral range. At large distances from the nucleus, $\gamma \approx 1$ when continuum contamination is negligible. Toward the center, γ decreases below unity and drops sharply in the innermost spaxels where the AGN continuum dominates.

Stellar kinematics were extracted from the JWST/NIRSpec G235H/F170LP data cube of M81 using the PPXF method (M. Cappellari 2023), focusing on the commonly used CO band head absorption features (e.g., M. Cappellari et al. 2009; D. Krajnović et al. 2018; D. D. Nguyen et al. 2018; S. Thater et al. 2023). As demonstrated by D. D. Nguyen et al. (2025b, 2026), LOSVDs derived using the empirical X-shooter Spectral Library (XSL;[10] 830 spectra from 683

[9] v8.2.1: https://pypi.org/project/ppxf/

[10] Data Release 3: http://xsl.u-strasbg.fr.

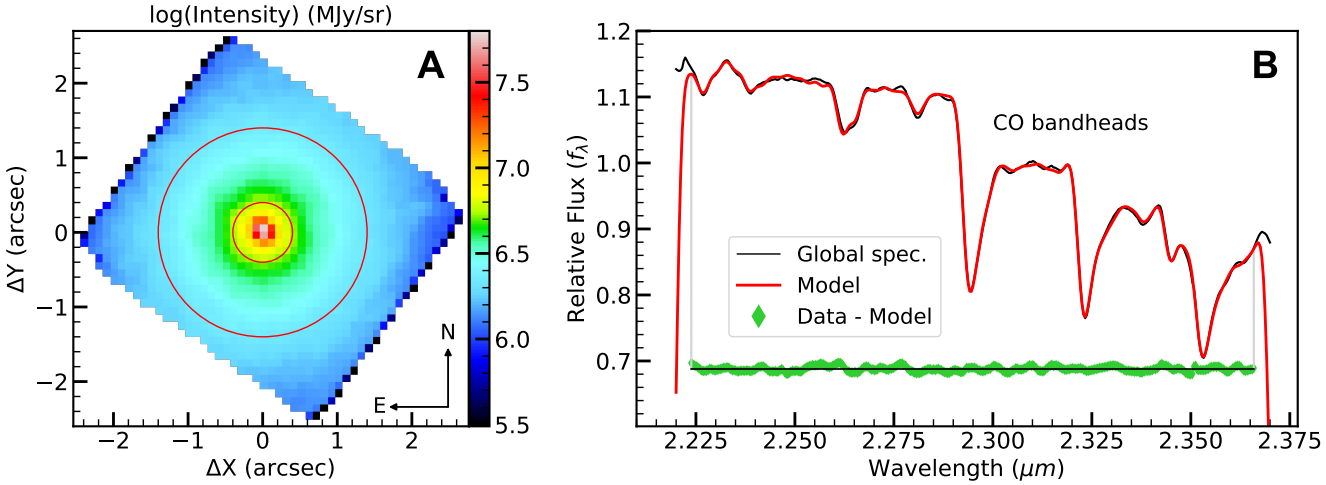

Figure 2. Panel (A): logarithmically scaled intensity map of the NIRSpec G235H/F170LP data cube, collapsed along the spectral axis (excluding the detector gap at 2.41–2.49 μm). The red circular annulus ($0\farcs4 < r < 1\farcs4$) indicates the region from which the global spectrum was extracted. Panel (B): the observed global spectrum (black) overlaid with the best-fit stellar template (red) for M81. The fit residuals (data – model) are shown in green and vertically offset by +0.62 to compress the y-axis range and better illustrate the stellar CO absorption band heads. This same vertical offset is applied to all subsequent figures of this type.

stars; K. Verro et al. 2022) agree within 3% of those obtained from the higher-resolution PHOENIX synthetic library (T.-O. Husser et al. 2013). The LOSVD based on XSL is thus adopted as our primary kinematic measurements throughout our analysis. The XSL covers 3000–25000 Å at $R \sim 10{,}000$, includes O–M and evolved stars, and has been corrected for extinction.

We followed the method of M. Cappellari et al. (2009) to separate the stellar light from the nonthermal AGN continuum in the nucleus of M81. This process requires an optimal XSL template, derived from a large spatial region of the nucleus to avoid kinematic bias (A. Marconi et al. 2000; J. D. Silge & K. Gebhardt 2003) caused by the AGN continuum. To determine an optimal description of the AGN continuum, we explored PPXF fits using additive (`degree`) and multiplicative (`mdegree`) Legendre polynomials spanning orders of 2–8. We find that the recovered stellar kinematics converge for `degree` $\geqslant 4$ and `mdegree` $\geqslant 4$, becoming insensitive to both the polynomial configuration and the adopted fitting window (2.225–2.370 μm; see Figures 2 and 3). We therefore adopt `degree` = 4 and `mdegree` = 4 as our fiducial setup, as this minimal choice adequately captures the AGN continuum and template mismatch while ensuring stable LOSVD recovery. The resulting LOSVDs are nearly identical beyond $0\farcs2$ for all tested configurations, while within this radius they differ by <3% for `degree` $\geqslant 4$ and `mdegree` $\geqslant 4$, increasing to ∼10% for lower-order choices. The resulting LOSVDs are nearly identical beyond $0\farcs2$, with differences within this radius remaining below 7.5%. These polynomials effectively capture low-order variations in line strength, residual sky-subtraction errors, spectral calibration imperfections, and AGN continuum contamination, allowing for robust measurements of the stellar velocity dispersion even in the central spaxels where AGN light dominates over the stellar CO band heads.

2.5. Determining the Optimal Stellar Template

First, we constructed a global spectrum by combining all spaxels within an annulus of $0\farcs4 < r < 1\farcs4$ (confined by the two red rings in the left panel of Figure 2) of the NIRSpec G235H/F170LP data cube, thereby excluding the central, AGN-contaminated spaxels. This annular spectrum achieves an S/N of 300 per spectral pixel and was logarithmically rebinned along the spectral dimension with a constant velocity scale of 50 km s^{-1} pixel^{-1} calculated using Equation (8) of M. Cappellari (2017).

Second, we accounted for the instrumental broadening of the spectrum in the XSL templates by convolving them with a Gaussian whose dispersion is determined using Equation (5) of M. Cappellari (2017).

Third, we derived the fixed optimal XSL template by fitting the XSL-instrumental-broadened spectra to the global spectrum using PPXF, modeling the LOSVD as a simple Gaussian by setting `moments` = 2. This setup returns the LOSVD parameters, including the rotational velocity V (relative to the systemic velocity $V_{\rm sys}$) and the velocity dispersion σ, which are our primary kinematic quantities of interest.

The fixed optimal XSL template, returned by PPXF, is composed 14 giant-star spectra, which reproduce the observed spectrum over 2.22–2.37 μm, including the CO band head absorption (right panel of Figure 2). The fit is dominated by the K4III C star (HD 109871 from XSL), contributing ≈45% of the flux, with additional contributions from a giant M2V C star (HIP 75423, ≈18%) and an M9 D star (BMB 289, ≈10%) required to match the data. From this template, PPXF yields $V = -31 \pm 3$ km s^{-1} and $\sigma = 168 \pm 4$ km s^{-1}, consistent with long-slit measurements at Calar Alto Observatory (R. Bender et al. 1994). The 1σ uncertainties are estimated from the standard deviation of 200 Monte Carlo realizations (M. Cappellari & E. Emsellem 2004).

2.6. Separating the Active Galactic Nucleus Continuum from Stellar Light

In this section, we assess the reliability of the fixed optimal stellar template (Section 2.4) for extracting stellar kinematics in the presence of nonthermal AGN emission within the NIRSpec G235H/F170LP data cube. To do so, we constructed high-S/N spectra by coadding spaxels within multiple concentric annuli spanning radii from $0\farcs1$ to $1\farcs7$. Each annular spectrum was then fit using the fixed optimal stellar template within the PPXF framework.

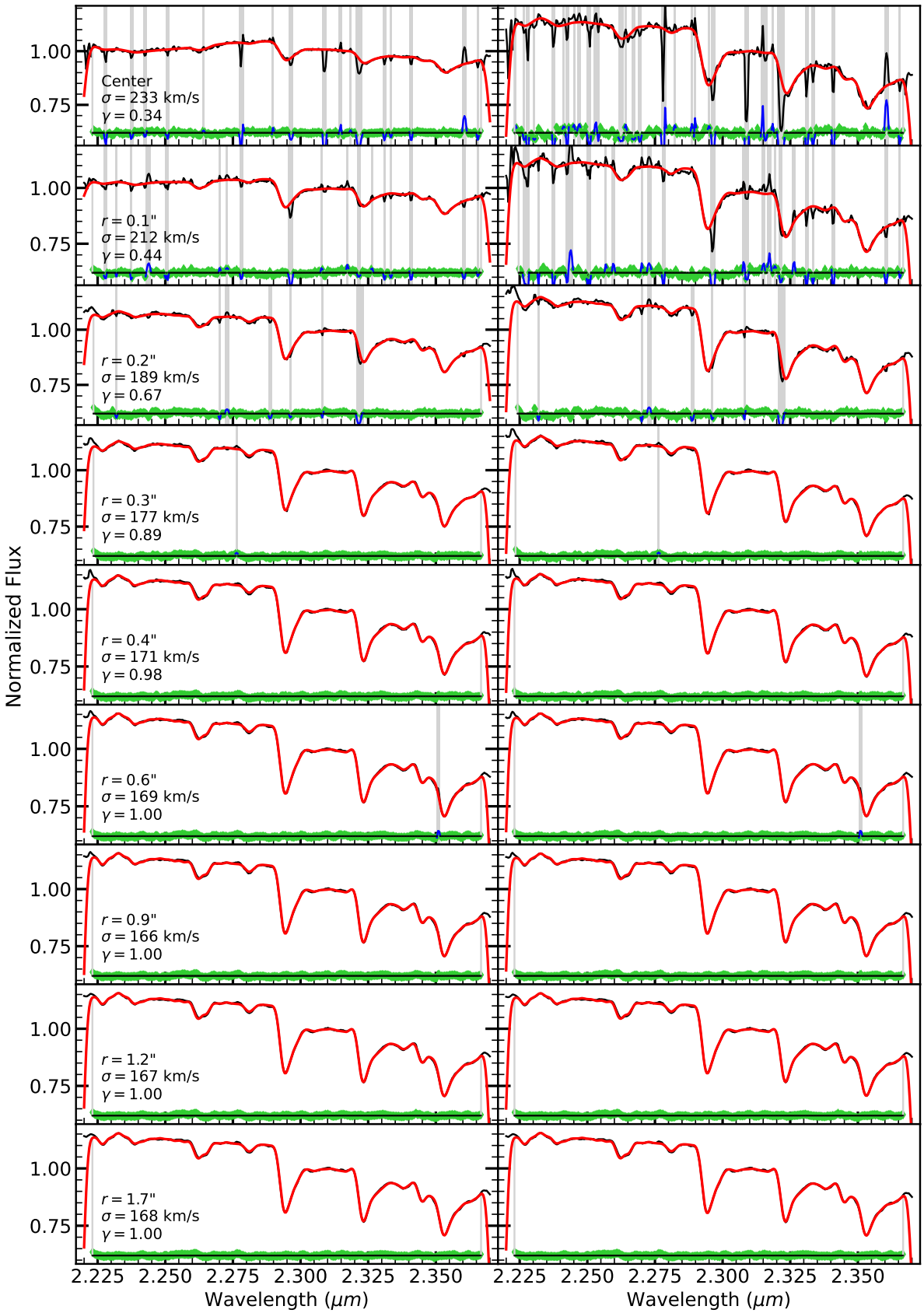

Figure 3. Radial spectral variation in M81 from the NIRSpec G235H/F170LP data cube. Left column: observed spectra (black line) obtained by coadding spaxels within concentric annuli at radius *r*. The overplotted red line shows the PPXF fit, which combines the global stellar template (see left panel of Figure 2 and Section 2.4), convolved with a Gaussian LOSVD and added by fourth-degree additive and multiplicative polynomials to account for the nonthermal nuclear continuum. Fit residuals (data – model) are shown in green, with regions masked due to emission lines or artifacts indicated in gray. Right column: the convolved stellar template (red line) is compared to the observed spectrum after subtracting the modeled nonthermal continuum (black line).

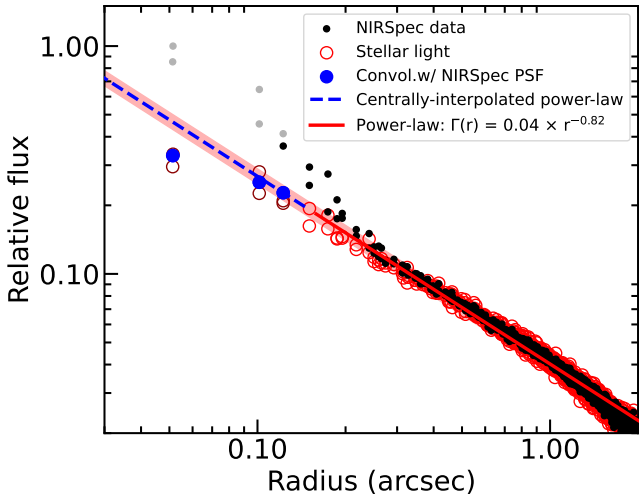

Figure 4. The radial surface-brightness profile $I(r)$, derived from individual Voronoi bins in the NIRSpec G235H/F170LP data cube of M81 (filled black circles), is compared to the estimated stellar-light profile $\Gamma(r) = I(r)\gamma(r)$ (red open circles). The underlying stellar distribution is smooth and well approximated by a single power law (red line with pink region shows its 1σ uncertainty). The PSF-convolved central interpolation of this single power law also reproduces the two innermost γ measurements, which lie below the intrinsic (unconvolved) profile, indicating that their apparent decline is fully consistent with PSF effects. Gray points indicate pixels where $\gamma < 0.5$.

Figure 3 shows the radial profiles of stellar line strength (γ, left) and stellar-light fraction (right). The observed spectra in each annulus are modeled with the fixed optimal stellar template plus fourth-degree additive and multiplicative Legendre polynomials to account for AGN continuum emission. The stellar-light fraction (right panels) is obtained by subtracting the AGN component, revealing a clear nonstellar contribution from the changing spectral slope. In the nucleus, the AGN contributes 66% of the flux, decreasing to ≈54% at $r \approx 0\farcs1$, ≈33% at $r \approx 0\farcs2$, and <10% beyond $r = 0\farcs2$.

We quantify the dilution of stellar light by the central nonthermal AGN continuum in Figure 4, which presents the radial surface-brightness profile $I(r)$ measured from the JWST/NIRSpec G235H/F170LP data cube of M81, together with the stellar contribution $\Gamma(r) = I(r)\gamma(r)$ derived from the PPXF fits in individual spatial bins. Similar analyses have been carried out for nearby systems such as M87 (Figure 4 of R. P. van der Marel 1994), Centaurus A (Figure 6 of M. Cappellari et al. 2009), and more recently M106 (Figure 4 of D. D. Nguyen et al. 2026). As an initial approximation in Figure 4, we modeled the radial stellar-light distribution using a single power-law form, $\Gamma(r) = \alpha \times r^{\beta}$ (red line), with $\alpha = 0.04$ and $\beta = -0.82$. This simple model overestimates the stellar-light fraction within $0\farcs1$ (blue dashed line), as it neglects the effect of the JWST/NIRSpec PSF at 2.3 μm.

To assess the impact of PSF convolution, we performed a forward-modeling experiment. First, we generated a synthetic image with an intrinsic surface-brightness profile $\Sigma \propto r^{-0.82}$, sampled at $0\farcs025\,\mathrm{pixel}^{-1}$, corresponding to a factor of 4 oversampling relative to the native NIRSpec spatial scale (PSF1 in Table 1 of D. D. Nguyen et al. 2026). This image was then convolved with the synthetic NIRSpec PSF at the same sampling and subsequently rebinned to the native scale of $0\farcs1\,\mathrm{pixel}^{-1}$ by summing 4×4 spaxels. We then measured the stellar fraction in the central spaxel of the rebinned image.

The resulting central stellar fraction follows the same trend defined by the three innermost measurements of $\gamma(r)$ in Figure 4, demonstrating that the apparent break toward the nucleus is fully accounted for by PSF convolution and spatial sampling effects. This behavior does not imply a genuine change in the intrinsic stellar surface-brightness profile within the NIRSpec FOV, but rather reflects instrumental effects that are properly accounted for once the PSF is taken into consideration. The determination of $\gamma(r)$ therefore enables a robust extraction of stellar kinematics even in the unresolved nuclear region, where stellar light is strongly diluted by AGN emission.

Although stars contribute only ∼34% of the total flux in the central spaxel, the resulting kinematics remains usable, albeit with larger systematic uncertainties of order ∼15%, and are thus retained in our dynamical modeling (Section 4.1). At radii beyond $r = 0\farcs1$, the stellar contribution increases and the kinematic measurements are correspondingly more secure, with typical uncertainties below 3%.

2.7. Two-dimensional Kinematic Maps

The 2D stellar LOSVD of the nucleus of M81 was derived following the fitting procedure described in Section 2.4. First, the adaptive Voronoi binning method[11] (M. Cappellari & Y. Copin 2003) was applied to spatially group spaxels until a target S/N of 150 per spectral pixel was achieved, resulting in $N = 700$ Voronoi bins. This target S/N represents a compromise: spaxels beyond $r \approx 0\farcs5 \approx r_{\mathrm{SOI}}$ were grouped, while those within this radius remained unbinned to preserve the spatial resolution necessary for precise stellar-kinematic measurements inside r_{SOI}. Within the SOI, individual unbinned spaxels exhibit S/N values ranging from 150 to 200 per spectral pixel, increasing toward the central peak. Each binned spectrum was resampled onto a logarithmic wavelength scale. The PPXF routine was then used to fit each binned spectrum with the fixed optimal XSL-instrumental-broadened template (Section 2.5), incorporating fourth-degree multiplicative and additive Legendre polynomials to derive the LOSVD (i.e., V and σ).

Figure 5 presents a logarithmic integrated intensity map (panel (A)), with a marked spaxel corresponding to the spectrum and a PPXF fit shown in panel (B). The remaining panels display the resulting maps of rotational velocity V (panel (C)), velocity dispersion σ (panel (D)), rms velocity $V_{\mathrm{rms}} = \sqrt{V^2 + \sigma^2}$ (panel (E)), and stellar line strength γ (panel (F)). The nucleus exhibits a steeply rising rotation, with $|V| \approx 40 \pm 4$ km s^{-1} at the edge of the NIRSpec IFU field (after subtracting the systemic heliocentric velocity of $v_{\mathrm{sys}} = -32 \pm 4$ km s^{-1}), consistent with the IFS observations by A. Schnorr Müller et al. (2011), as expected for a spiral galaxy. This derived v_{sys} from the JWST/NIRSpec G235H/F170LP data cube is 7 km s^{-1} larger than the value reported in the NASA/IPAC Extragalactic Database (NED).[12]

We measure a global kinematic position angle (PA) of $\mathrm{PA_{kin}} = 151\overset{\circ}{.}6 \pm 9\overset{\circ}{.}5$. Both v_{sys} and $\mathrm{PA_{kin}}$ were derived from the velocity map using the PAFIT[13] package (D. Krajnović et al. 2006). The kinematic $\mathrm{PA_{kin}}$ is consistent within the uncertainties with the photometric one $\mathrm{PA_{phot}} \approx 157°$ reported

[11] v.3.1.5: https://pypi.org/project/vorbin/
[12] https://ned.ipac.caltech.edu
[13] v.2.0.8: https://pypi.org/project/pafit/

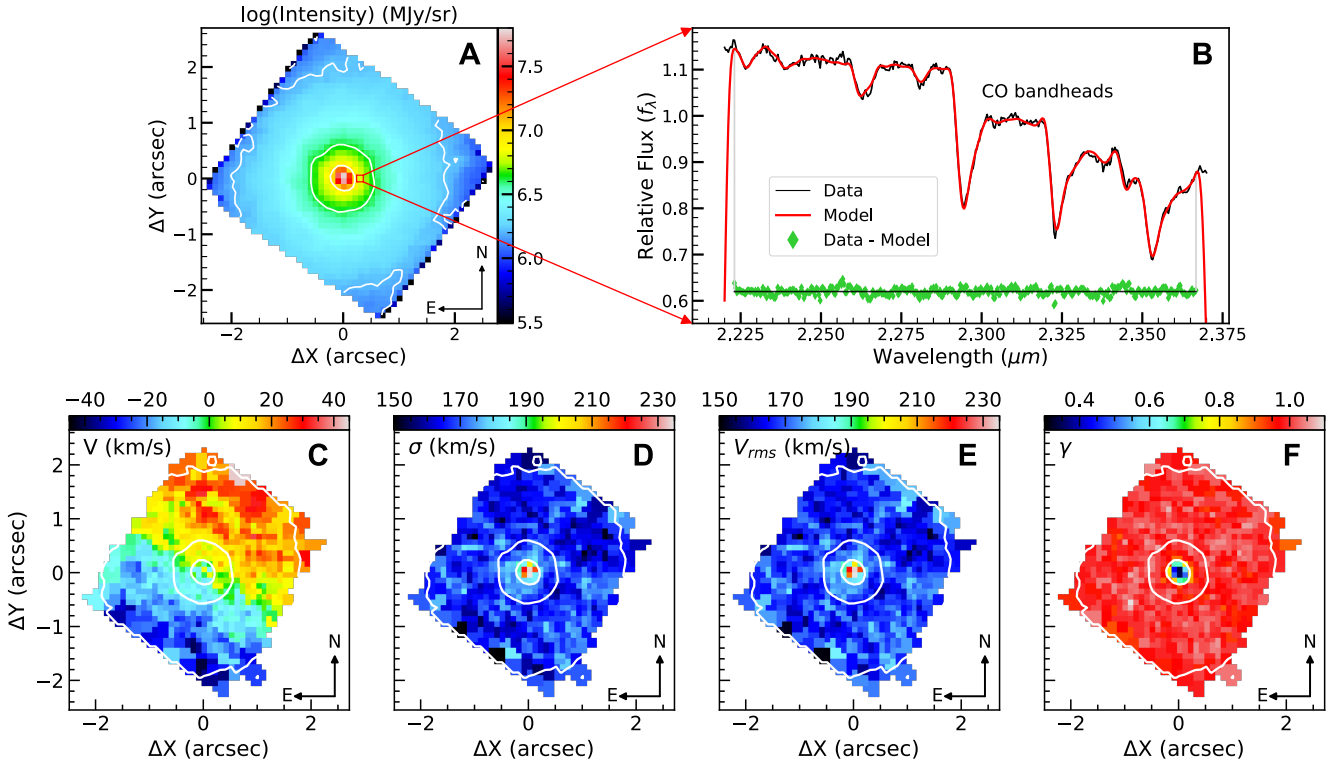

Figure 5. Stellar-kinematic measurements from the NIRSpec G235H/F170LP observations of NGC 3031 are shown. Panel (A): the logarithmic collapsed intensity map (see left panel of Figure 2). Panel (B): example PPXF fit for a central-offset Voronoi bin unaffected by wiggles (location indicated in panel (A)). The observed spectrum (black) displays the CO band head absorption near 2.3 μm, with the best-fit XSL template overplotted in red. Fit residuals (data – model) are plotted in green, and the vertical gray lines mark the wavelength range used for fitting across all bins. Panels (C)–(F): 2D maps of the of the stellar rotation velocity (V), velocity dispersion (σ), rms velocity ($V_{\rm rms} = \sqrt{V^2 + \sigma^2}$), and stellar-light contribution fraction (γ), respectively. The central white pixels are masked due to unreliable kinematics, as the AGN continuum contributes ≈66% of the total light in this region. White contours trace the intensity, decreasing by magnitude per arcseconds steps from the center.

in the HyperLeda database[14] (G. Paturel et al. 2003), as expected for a nearly axisymmetric disk galaxy. The σ profile, which dominates over V, rises from $\sim$165 $\pm$ 4 km s^{-1} at $r \gtrsim 1''$ (≈3 km s^{-1} higher than the value obtained from GMOS observations by A. Schnorr Müller et al. 2011), to a central peak of $\sim$233 $\pm$ 15 km s^{-1} within $r \lesssim 0\farcs1$. This central increase in both σ and $V_{\rm rms}$ provides strong evidence for the presence of a central SMBH. We presented these stellar-kinematic measurements in Table 1.

As shown in panel (F) of Figure 5, the nonthermal AGN continuum exhibits only weak emission, with $\gamma \approx 1$ over most of the NIRSpec FOV, except within the innermost spaxels where $\gamma \leqslant 0.34$. In these central spaxels, the AGN light dominates, resulting in relatively large kinematic uncertainties of up to $\sim$15%. In contrast, for the remaining bins—where the stellar light contributes more than 34% of the total flux—the derived stellar kinematics is robust, with uncertainties below 3%.

Table 1
JWST/NIRSpec Kinematic Data of the M81 Nucleus

ΔR.A. (arcsec)	ΔDecl. (arcsec)	V (km s^{-1})	ΔV (km s^{-1})	σ (km s^{-1})	$\Delta\sigma$ (km s^{-1})
0.012	0.050	7.66	14.16	233.77	14.05
0.112	0.050	−9.08	6.79	216.17	8.66
0.012	−0.150	−11.06	5.02	180.76	6.33
0.212	0.050	10.43	3.76	179.11	4.72
−0.188	0.150	8.23	3.82	188.36	4.80
−0.088	−0.250	−12.29	3.46	174.71	4.33
−0.288	−0.050	−9.06	3.29	172.81	4.12

Note. (This table is available in its entirety in machine-readable form. A portion is shown here for guidance regarding its form and content. A data copy is also available in Zenodo at DOI: 10.5281/zenodo.18345300).

(This table is available in its entirety in machine-readable form in the online article.)

2.8. NIRSpec Active Galactic Nucleus Point-spread Function at 2.3 μm

From panel (F) of Figure 5, we derive the AGN light fraction map as $1 - \gamma$, where γ denotes the stellar-light fraction. The AGN light-distribution map, shown in the lower panel of Figure 6, is then obtained by multiplying this fraction map by the integrated-light map from the JWST/NIRSpec G235H/F170LP data cube. We parameterize the resulting AGN light distribution using a multi-Gaussian expansion (MGE; E. Emsellem et al. 1994), implemented with the `mge_fit_sector` routine from the MGEFIT package (M. Cappellari 2002). The 2D AGN light distribution is expressed analytically as

$$\mathrm{PSF}_{\rm AGN}(r) = \sum_{j=1}^{n} \frac{F_j}{2\pi\sigma_j^2} \exp\left(-\frac{r^2}{2\sigma_j^2}\right),$$

where r is the radial coordinate, σ_j is the dispersion of Gaussian component j, and F_j is its normalized weight, with

[14] https://leda.univ-lyon1.fr/

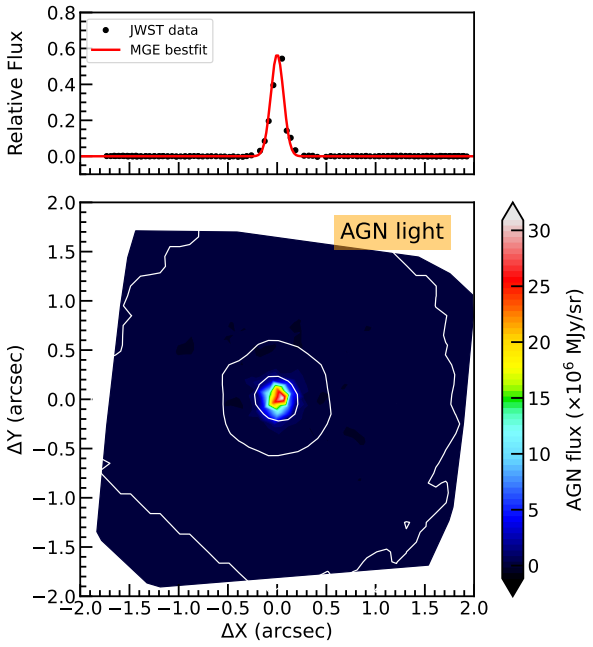

Figure 6. Upper panel: the 1D radial profiles of the spectrally extracted AGN signal from the JWST/NIRSpec G235H/F170LP data cube, shown together with the best-fitting MGE model of the PSF. The profile is constructed by mapping each data point to its projected radius, with negative and positive values corresponding to positions on opposite sides of the nucleus. Lower panel: the 2D image of the extracted AGN light distribution displayed on a logarithmic scale.

$\sum_{j=1}^{n} F_j = 1$. The best-fit MGE PSF model for the AGN light distribution comprises two Gaussians, which have an average FWHM of 0.″21, as listed in Table 2 and shown in the upper panel of Figure 6. This value is consistent with the STPSF synthetic JWST/NIRSpec PSF reported in Table 1 of D. D. Nguyen et al. (2026) and with the empirical PSF derived by M. C. Bentz (2025) from observations of an isolated late-type star. We adopt this PSF model in this work to derive the BH mass of M81 (Section 4.2).

3. Imaging and Photometric Model

Accurate dynamical modeling and $M_{\rm BH}$ measurements require a well-constrained estimate of the gravitational potential of the galaxy. We derived the stellar potential by scaling the galaxy's luminosity with a mass-to-light ratio (M/L). To model the stellar luminosity distribution with high fidelity, we combined high-resolution narrow-field space-based HST imaging with wide-field ground-based data from the 2MASS survey.

3.1. HST Observation and Its Point-spread Function Image

We modeled the stellar-light distribution of M81 within a $110'' \times 110''$ field using HST imaging obtained on 2009 June 24 with the WFC3/IR channel, which has a pixel scale of 0.″09, and the broadband F110W filter. The observation consists of a single exposure with a total on-source integration time of 143 s.

We required a PSF to deconvolve the HST image into the intrinsic stellar-light distribution (Section 3.5). We generated a synthetic PSF using the `Tiny Tim` software package[15]

[15] https://github.com/spacetelescope/tinytim

Table 2
JWST/NIRSpec Active Galactic Nucleus Multi-Gaussian Expansion Point-spread Function Model at 2.3 μm and HST `Tiny Tim` WFC3/F110W Multi-Gaussian Expansion Point-spread Function Model

j	(Light fraction)$_j$	σ_j (arcsec)	FWHM$^{\rm tot}_{\rm PSF}$ (arcsec)
		PSF$_{\rm AGN}$	
1	0.770	0.080	0.210
2	0.230	0.128	...
		PSF$_{\rm HST}$	
1	0.442	0.028	0.131
2	0.389	0.094	...
3	0.099	0.330	...
4	0.070	0.825	...

Note. The first column gives the number of Gaussian components. The second column reports the light fraction of each Gaussian. The third column lists the Gaussian dispersions along the major axis. The fourth column lists the representative average FWHM of the HST photometric PSF, computed from their Gaussian components.

(J. Krist 1995; J. E. Krist et al. 2011), specifically employing the `tiny1` and `tiny2` routines, which simulate the PSF for a given filter, detector chip, chip position, and instrument configuration. To ensure consistency with the actual observations, the PSF was generated using the same exposure parameters as the HST image, and was subsequently convolved with an appropriate charge diffusion kernel to account for the redistribution of electrons into neighboring pixels on the detector.

3.2. 2MASS

To characterize the stellar-light distribution of M81 beyond the central $110'' \times 110''$ region, we used a large-scale J-band image from the 2MASS survey, which covers the wavelength range of 1.12–1.36 μm and has a central wavelength of 1.235 μm (T. H. Jarrett et al. 2003). The 2MASS image has a pixel scale of $1''$ pixel^{-1}.

3.3. Center Offset in the HST F110W Image?

We determined the photometric center of the HST/IR F110W image by measuring the light centroid within a $1'' \times 1''$ region and compared it to the reference weighted barycenter derived from the JWST/NIRSpec data (Section 2.3). The two centers differ by only $\sim$0.″09 toward the southwest (Figure 7), which is slightly smaller than the spatial resolution of both datasets ($\sim$0.″1), indicating consistency within the observational uncertainties. Since this offset is present in the F110W image but not in the JWST/NIRSpec data, it is unlikely to be caused by dust extinction.

However, the S/N in the HST image is sufficiently high to verify that the AGN peak is well aligned with the offset brightness peak. This offset may therefore be interpreted as possible morphological evidence that the SMBH has not yet fully settled at the center. There are not many galaxies that are close enough for us to resolve such an offset between the SMBH's location and the photometric center, except for the well-known example of the M31 nucleus (T. R. Lauer et al. 2005) and the recent same discovery in the nucleus of NGC 4486B in the Virgo Cluster (B. Tahmasebzadeh et al. 2025).

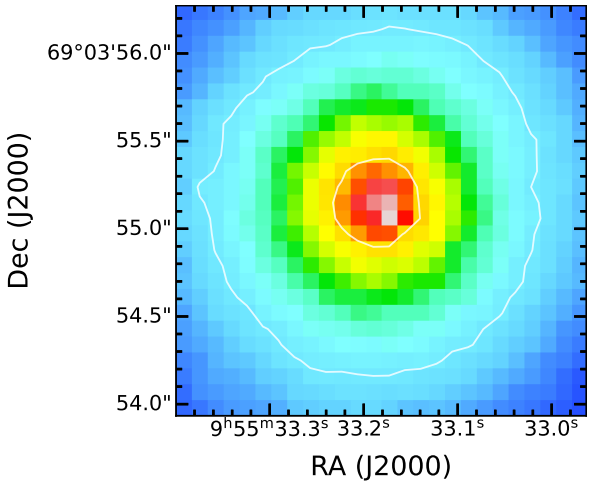

Figure 7. The central region of the HST/WFC3 F110W image reveals a peak in surface brightness that is offset by approximately 0.″1 to the southwest of the M81 nuclear centroid.

Spatial or kinematic offsets between the location of the SMBH and the photometric or dynamical center of a galaxy have been reported in several nearby systems and interpreted in a variety of contexts. A classic example is the double nucleus of M31, in which the brighter off-center component (P1) and the true nucleus (P2) can be understood as asymmetric stellar structures in an eccentric disk around the central BH (T. R. Lauer et al. 2005), and measurements indicate a small displacement of the SMBH from the bulge center consistent with this model (e.g., T. R. Lauer et al. 1998; J. Kormendy & R. Bender 1999). Similarly, early HST studies suggested a projected offset of $\sim$0.″1 in M87 between the nuclear point source and the galaxy photocenter, though subsequent work attributed much of this apparent displacement to temporal jet variability rather than a true SMBH displacement (e.g., D. Batcheldor et al. 2010). Searches for recoiling or displaced SMBHs in samples of nearby early-type galaxies have also found modest ($\lesssim$10 pc) AGN-photocenter separations in a fraction of objects, which can be explained by postmerger recoil oscillations or asymmetric jet acceleration (e.g., D. Lena et al. 2014). Observations of velocity-offset AGN emission lines further suggest that kinematic displacements in ionized gas can arise from outflows, dual nuclei, or eccentric nuclear structures (e.g., F. Müller-Sánchez et al. 2016). More recent cosmological simulations indicate that off-center SMBHs, particularly in brightest cluster galaxies, may be common outcomes of hierarchical assembly, with roughly one-third of systems showing significant displacements at $z = 0$ due to merger dynamics (e.g., Q. Chu et al. 2022). These studies together demonstrate that while exact SMBH–galaxy center coincidence is the norm, small offsets do occur and can provide clues to recent dynamical history beyond simple noise or measurement uncertainty.

3.4. Separating Central Active Galactic Nucleus Emission from Stellar Light in the HST image

Our galaxy mass model of M81 must represent the stellar-light distribution only, free from contamination by the central AGN. To achieve this, we corrected the HST/WFC3 IR F110W image by modeling and subtracting the AGN point source before fitting the MGE. Following the approach of D. A. Simon et al. (2024), we estimated the AGN's spatial profile from the NIRSpec stellar fraction map (γ; panel (F) of Figure 5), assuming minor differences between the HST/WFC3 IR F110W and JWST/NIRSpec G325H/F170LP PSFs are negligible. The fractional contribution of the AGN at a given radius is $(1 - \gamma)$. We modeled this radial profile by assuming the AGN light distribution can be approximated by a Gaussian function, which leads to the form

$$\gamma(r) = 1 - \Delta\gamma \cdot \exp\left(-\frac{r^2}{2\sigma^2}\right),$$

where the best-fit values are $\Delta\gamma = 0.612$ and $\sigma = 0.''131$ (left panel of Figure 8). Using this fit, we constructed a modified (i.e., AGN-free) HST/WFC3 IR F110W image in which the innermost subarcsecond region was replaced with the AGN-free stellar profile. The fitted profile was then matched to the original HST/WFC3 IR F110W surface-brightness profile (i.e., AGN + stars) beyond 0.″3 (right panel of Figure 8).

3.5. Full Surface-brightness Profile and Galaxy Mass Model of M81

Before constructing the 2D stellar surface-brightness distribution of M81, we estimated and subtracted the sky background in the 2MASS *J*-band images independently. The sky level was determined as the median signal measured within several $10 \times 10\,\mathrm{pixel}^2$ boxes placed in source-free regions at projected distances greater than 400″ from the galaxy center. This median value was then subtracted from the the image to produce a sky-subtracted frame used in the subsequent analysis. Regions affected by dust obscuration and foreground stars were masked in both the HST/WFC3 IR F110W and the sky-subtracted 2MASS *J*-band images before the fitting procedure.

We then constructed the 2D stellar surface-brightness distribution of M81 using the `mge_fit_sectors_regularized` routine from the MGEFIT package (see footnote 15), fitting the HST/WFC3 IR F110W and sky-subtracted 2MASS *J*-band images simultaneously. During the fitting process, we accounted for the HST/WFC3 IR F110W PSF to recover the galaxy's intrinsic light distribution. Specifically, the PSF image was first modeled as an MGE, whose parameters are listed in Table 2, with an FWHM of 0.″131, which was then convolved with the HST/WFC3 IR F110W image during the fit. This step is essential, as the accuracy of the M_{BH} measurement depends critically on how well the central stellar-mass distribution is modeled.

The procedure consisted of the following steps.

1. We extracted multisector surface-brightness profiles from the HST/F110W image (describing the inner regions) and from the sky-subtracted 2MASS *J*-band image (describing the outer regions). The central region of the sky-subtracted 2MASS image overlapping with the HST FOV was masked to avoid double counting and to prevent the lower-resolution data from influencing the inner profile.
2. We placed the two datasets on a consistent photometric scale. We used the `PhotometryMatch` routine to determine the relative flux offset and a multiplicative flux scaling factor between the HST and the sky-subtracted

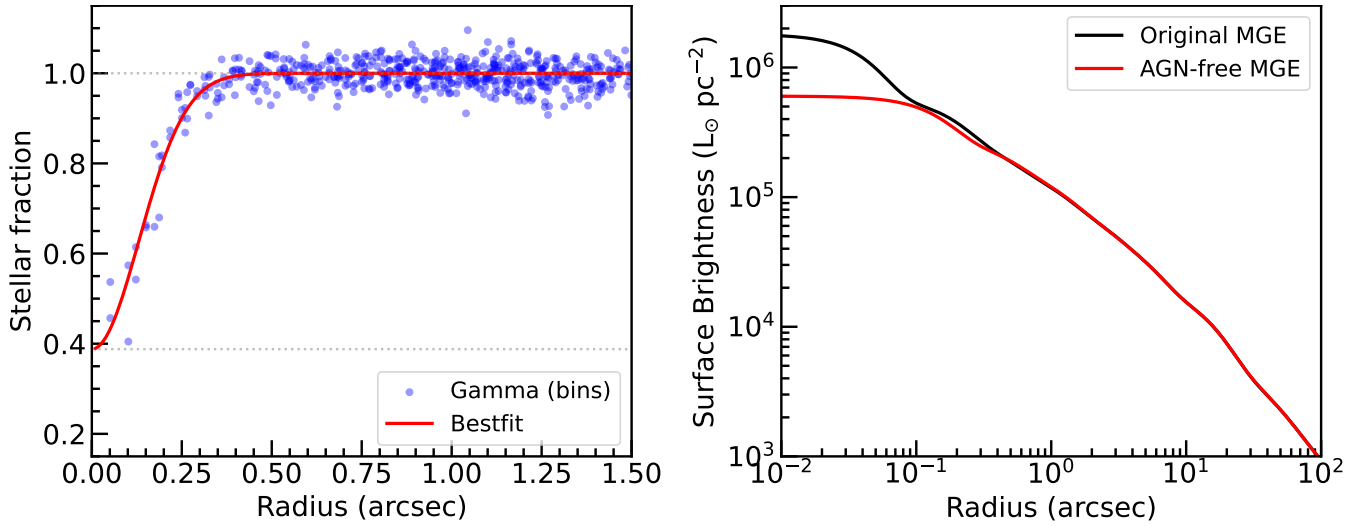

Figure 8. Left: the stellar-light fraction distribution for all kinematic bins measured in Section 2.7 and extracted from panel (F) of Figure 5. The red curve represents the best-fit profile, which dominates beyond 0.″3 but declines sharply toward the galaxy center. Right: comparison between the scaled HST radial profile (black line) and the profile constrained by the stellar contribution (red line) measured spectroscopically with JWST/NIRSpec G235H/F170LP.

2MASS profiles. These parameters were derived by minimizing the photometric residuals in an overlapping annulus between 5″ and 50″, where both datasets have a reliable signal. This step accounts for differences in pixel scale, absolute calibration, and background subtraction between the two images.

3. We combined the HST radial photometry at radii $r < 50''$ with the sky-subtracted 2MASS photometry at $r > 50''$ into a single, continuous surface-brightness profile.
4. We then applied MGEFIT to this combined profile, with PSF convolution applied only to the HST component. The resulting MGE therefore represents a joint fit to the inner high-resolution HST data and the outer wide-field 2MASS data, ensuring a smooth and physically consistent stellar-mass model across all radii.

Next, the flux units of counts per second were converted to physical units of $L_\odot$ pc^{-2} following the procedure outlined by D. Thatte et al. (2009), adopting photometric zero-points and absolute magnitudes for the Sun in the Vega system (C. N. A. Willmer 2018). For the HST image, we used $m_{0,\mathrm{F110W}} = 26.05$ mag[16] and $M_{\mathrm{Vega,F110W}} = 3.79$ mag; for the 2MASS image, $m_{0,J} = 20.92$ mag and $M_{\mathrm{Vega},J} = 3.67$ mag were adopted. Galactic extinction corrections of $A_{\mathrm{F110W}} = 0.071$ mag for the HST image (E. F. Schlafly & D. P. Finkbeiner 2011) and $A_J = 0.058$ mag[17] for the 2MASS image were also applied.

Both the original and modified HST images were then fitted with MGE models, which were subsequently matched to the 2MASS J-band MGE model at large radii. We list in Table 3 this combined and AGN-free MGE model, which consists of 14 concentric Gaussian components and has a somewhat flatter central profile (red line) compared to the AGN-contaminated one (black line), as seen in the right panel of Figure 8. It is clear that the AGN-contaminated stellar light near the nucleus is nonnegligible and, if uncorrected, would significantly bias the SMBH mass measurement for M81. Figure 9 presents this best-fitting, combined, and AGN-free MGE model overlaid on the observed surface-brightness distribution of M81, based on the 2MASS J-band image (left) and the HST WFC3/IR F110W image (middle). A zoom-in view of the central $10'' \times 10''$ region from the HST WFC3/IR F110W image is shown in the right panel. This figure demonstrates that the combined MGE model accurately reproduces the galaxy's isophotes across a broad range of spatial scales, confirming its suitability for subsequent dynamical modeling.

In the subsequent dynamical analysis of M81, we adopted this best-fitting, combined, and AGN-free MGE model as the fiducial stellar-mass model, while the similar best-fitting and combined but AGN-contaminated MGE model was used to assess the systematic uncertainties.

Table 3
Gaussian Parameters of the M81 Multi-Gaussian Expansion Model

j	$\log(\Sigma_{\star,j})$ ($L_\odot$ pc^{-2})	$\log(\sigma_j)$ (arcsec)	$q'_j(=b/a)$
1	5.511	−0.940	0.727
2	5.034	−0.468	0.900
3	4.873	−0.107	0.900
4	4.610	−0.194	0.900
5	4.172	0.543	0.681
6	4.280	0.569	0.900
7	4.007	1.020	0.550
8	3.630	1.112	0.843
9	3.234	1.374	0.621
10	3.207	1.516	0.717
11	3.070	1.754	0.766
12	2.783	2.078	0.500
13	2.353	2.391	0.500
14	1.497	2.468	0.900

Note. The first column gives the number of Gaussian components. The second column reports the surface brightness of each Gaussian. The third column lists the Gaussian dispersions along the major axis. The fourth column provides the corresponding axis ratios.

[16] https://www.stsci.edu/files/live/sites/www/files/home/hst/instrumentation/wfc3/documentation/instrument-science-reports-isrs/_documents/2024/WFC3-ISR-2024-13.pdf
[17] https://irsa.ipac.caltech.edu/applications/DUST/

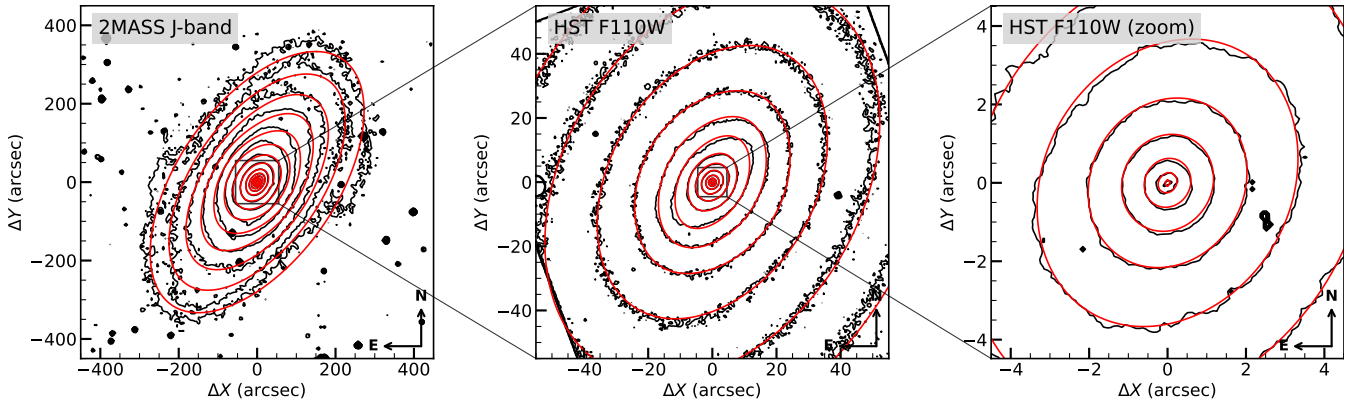

Figure 9. Left: isophotes of M81 from the 2MASS J-band image (black contours) and the corresponding MGE model (red contours) are shown over a $1000'' \times 1000''$ FOV. Middle: the same comparison is presented for the HST/WFC3/IR F110W image, covering a $110'' \times 110''$ FOV. Right: zoom-in view of the central $10'' \times 10''$ region of the HST image. The MGE model accurately reproduces the observed isophotes across all spatial scales. Contours represent decreasing surface-brightness levels, with a spacing of 1 mag arcsec^{-2}.

The 2D light distribution is then deprojected, assuming an axisymmetric potential and a free inclination angle (i), to yield a 3D axisymmetric luminosity profile. By multiplying this luminosity distribution by the M/L_J ratio in the J band, we obtain a model of the mass density, from which the gravitational potential can be calculated via the Poisson equation.

4. Dynamical Modeling

4.1. Jeans Anisotropic Models

We used both the cylindrically aligned JAMs (JAM$_{\rm cyl}$; M. Cappellari 2008) and the spherically aligned version (JAM$_{\rm sph}$; M. Cappellari 2020), each assuming an axisymmetric potential, to assess how velocity-ellipsoid alignment affects the dynamical $M_{\rm BH}$ determination in M81 by comparing the observed NIRSpec G235H/F170LP $V_{\rm rms}$ map with model predictions.

The JAM$_{\rm cyl}$ aligns the velocity ellipsoid with cylindrical coordinates (R, ϕ, z). The anisotropy is described by $\beta_z = 1 - (\sigma_z/\sigma_R)^2$. In contrast, the JAM$_{\rm sph}$ model aligns the velocity ellipsoid with spherical coordinates (r, θ, ϕ). Here, the anisotropy is quantified by $\beta_r = 1 - (\sigma_\theta/\sigma_r)^2$. In both models, all three components of the velocity ellipsoid are allowed to be different.

We constructed our models using the `jam.axi.proj` routine in JAMPY[18] (M. Cappellari 2020), setting `align = 'cyl'` for cylindrical alignment and `align = 'sph'` for spherical alignment to compute the LOSVD moments $\langle V_{\rm los}^2 \rangle$.

4.2. Model Grid and Parameter Space

Both JAM$_{\rm cyl}$ and JAM$_{\rm sph}$ estimate $M_{\rm BH}$ (sampled logarithmically) and additional parameters (sampled linearly), including the mass-to-light ratio (M/L_J) and the orbital anisotropy. In JAM$_{\rm sph}$, the radial anisotropy (β_r) is parameterized as the ratio σ_θ/σ_r, whereas in JAM$_{\rm cyl}$, the vertical anisotropy (β_z) is defined as the ratio σ_z/σ_R. In the JAM$_{\rm cyl}$ models, we adopted a constant anisotropy with no imposed priors. For the physically motivated JAM$_{\rm sph}$ models, we implemented the D. A. Simon et al. (2024) logistic anisotropy prescription with the priors described in Section 4.4. For the inclination parameter (i; converted to $q_{\rm min}$), we fixed it to the photometrically determined value of $i \simeq 63°$ ($q_{\rm min} \approx 0.05$), as M81 is a spiral galaxy with a relatively low and well-constrained inclination inferred from its dust-lane morphology. Allowing for near edge-on configurations is clearly inconsistent with the observed photometry and was therefore not considered. The adopted inclination is taken from the HyperLEDA database.[19]

In these JAMs, we accounted for the effects of the NIRSpec G235H/F170LP PSF at 2.3 μm, testing both synthetic and empirical PSFs. D. D. Nguyen et al. (2026) showed that synthetic PSF1 (FWHM$^{\rm tot}_{\rm PSF} = 0\farcs08$) and PSF2 (FWHM$^{\rm tot}_{\rm PSF} = 0\farcs15$) provide good fits to the JWST/NIRSpec stellar kinematics of NGC 4258, while PSF3 (FWHM$^{\rm tot}_{\rm PSF} = 0\farcs20$) underestimates the central $V_{\rm rms}$ by $\approx$20 km s^{-1}. We also tested empirical NIRSpec IFU PSFs constrained by F. D'Eugenio et al. (2024, 2026), which are consistent with our PSF2, whereas those reported by M. C. Bentz (2025) and our AGN-based PSF derivation in Section 2.8 are both consistent with our synthetic PSF3. In addition, we explored both constant and radially varying M/L_J assumptions (Section 4.3) to assess systematic uncertainties in the $M_{\rm BH}$ measurement of M81.

In total, we performed 12 JAM runs as listed in Table 4 and summarized below, which together bracket the main sources of systematic uncertainty in our dynamical analysis.

1. *Anisotropy alignment (two options).* Either cylindrically aligned velocity ellipsoid (JAM$_{\rm cyl}$) or spherically aligned one (JAM$_{\rm sph}$).
2. *PSF (three options).* Three STPSF (M. Perrin et al. 2025) synthetic JWST/NIRSpec PSFs were tested (Table 1 of D. D. Nguyen et al. 2026).
3. *Mass-to-light ratio (two options).* Either a constant M/L_J or a radially varying M/L_J within the NIRSpec FOV data cube (Section 4.3).

4.3. Linearly Varying M/L$_{\rm J}$ Profile

Possible population variation within the nucleus of M81 can bias both the central M/L_J and $M_{\rm BH}$ measurements. We performed an additional test, in which the M/L_J values beyond

[18] v7.2.0: https://pypi.org/project/jampy/

[19] http://atlas.obs-hp.fr/hyperleda/

Table 4
Summary of the 12 Jeans Anisotropic Models Best-fitting Parameters and Formal Uncertainties

M/L_J	$\mathrm{FWHM}_{\mathrm{PSF}}^{\mathrm{tot}}$ (arcsec)	M_{BH} ($\times 10^7\ M_\odot$)	M/L_J ($M_\odot/L_\odot$)	$M/L_J^{0''}$ ($M_\odot/L_\odot$)	$M/L_J^{2''}$ ($M_\odot/L_\odot$)	σ_z/σ_R	$(\sigma_r/\sigma_\theta)_0$	$(\sigma_r/\sigma_\theta)_\infty$
(1)	(2)	(3)	(4)	(5)	(6)	(7)	(8)	(9)
				$\mathrm{JAM}_{\mathrm{cyl}}$ models with constant anisotropy				
Constant	0.08	5.14 ± 0.24	1.76 ± 0.03	…	…	1.00 ± 0.01	…	…
Constant	0.15	5.01 ± 0.23	1.77 ± 0.03	…	…	1.00 ± 0.01	…	…
Constant	0.20	4.89 ± 0.23	1.77 ± 0.03	…	…	1.00 ± 0.01	…	…
Varying	0.08	4.99 ± 0.23	…	1.89 ± 0.09	1.72 ± 0.03	1.00 ± 0.01	…	…
Varying	0.15	4.66 ± 0.22	…	2.01 ± 0.09	1.69 ± 0.03	1.00 ± 0.01	…	…
Varying	0.20	4.75 ± 0.22	…	1.89 ± 0.10	1.73 ± 0.04	1.00 ± 0.01	…	…
				$\mathrm{JAM}_{\mathrm{sph}}$ models with radially varying logistic anisotropy				
Constant	0.08	4.80 ± 0.46	1.73 ± 0.08	…	…	…	1.00 ± 0.10	1.02 ± 0.05
Constant	0.15	4.68 ± 0.45	1.69 ± 0.09	…	…	…	0.99 ± 0.11	1.04 ± 0.05
Constant	0.20	4.54 ± 0.44	1.75 ± 0.11	…	…	…	1.00 ± 0.12	1.02 ± 0.06
Varying	0.08	4.82 ± 0.46	…	1.86 ± 0.60	1.73 ± 0.05	…	1.00 ± 0.14	1.00 ± 0.08
Varying	0.15	4.51 ± 0.43	…	2.02 ± 0.67	1.69 ± 0.05	…	1.00 ± 0.18	1.00 ± 0.09
Varying	0.20	4.53 ± 0.43	…	1.89 ± 0.93	1.73 ± 0.07	…	1.00 ± 0.26	1.00 ± 0.13

Note. Column (1): assumed M/L_J profile type. Column (2): total FWHM of the synthetic PSF model. Column (3): best-fit BH mass. Column (4): best-fit constant M/L_J. Columns (5) and (6): best-fit central and outer M/L_J for the varying profile, respectively. Column (7): best-fit vertical anisotropy for the $\mathrm{JAM}_{\mathrm{cyl}}$ models. Column (8): best-fit central radial anisotropy for the $\mathrm{JAM}_{\mathrm{sph}}$ models. Column (9): best-fit outer radial anisotropy for the $\mathrm{JAM}_{\mathrm{sph}}$ models.

the NIRSpec FOV ($r > 2''$) were fixed to the best-fit value obtained from the corresponding models with a constant M/L_J parameter. However, within $2''$, M/L_J was allowed to vary linearly toward a central value $\mathrm{M/L}_J^{0''}$.

In JAMs, the $M/L_J(r)$ profile is implemented by associating a different $(M/L_J)_j$ to each Gaussian component with dispersion σ_j in the MGE listed in Table 3, as follows:

$$\left(\frac{M}{L_J}\right)_j = \begin{cases} M/L_J^{0''} + \dfrac{M/L_J^{2''} - M/L_J^{0''}}{2''} \times \sigma_j, & \sigma_j < 2'', \\ M/L_J^{2''}, & \sigma_j \geqslant 2''. \end{cases} \tag{1}$$

4.4. Logistic Anisotropy for Spherical Jeans Anisotropic Models

While formally Jeans models are subject to the mass–anisotropy degeneracy (J. Binney & G. A. Mamon 1982), our understanding of galaxy dynamics has vastly improved since then. It now allows us to place physically motivated priors on the stellar orbital structure, significantly improving the reliability of the mass measurement. Both observations and simulations of massive galaxies consistently show a characteristic anisotropy profile: orbits are nearly isotropic or mildly radially biased at large radii, but become tangentially biased inside the BH's SOI. This orbital structure is thought to be a natural outcome of SMBH binary scouring during galaxy mergers, which preferentially ejects stars on radial orbits (e.g., M. Milosavljević & D. Merritt 2001; A. Rantala et al. 2024). While this scenario has been primarily studied in massive elliptical galaxies, the lack of radially biased orbits near the BH has also been observed in lower-mass fast-rotating systems (see a review of the observations in M. Cappellari 2026, Figure 10).

To capture this expected behavior, we explored the $\mathrm{JAM}_{\mathrm{sph}}$ model with a flexible, radially varying anisotropy, as done by D. A. Simon et al. (2024). This model uses a logistic function of $\log r$ to describe the radial anisotropy profile $\beta_r(r) = 1 - \sigma_\theta^2/\sigma_r^2$:

$$\beta_r(r) = \beta_{r,0} + \frac{\beta_{r,\infty} - \beta_{r,0}}{1 + (r_a/r)^\alpha}. \tag{2}$$

Here, $\beta_{r,0}$ and $\beta_{r,\infty}$ are the anisotropy values at the center and at large radii, respectively, and r_a is the transition radius. We reexpress the anisotropy in terms of the more intuitive velocity-dispersion ratio $\sigma_r/\sigma_\theta = 1/\sqrt{1-\beta_r}$.

Based on the established physics, we applied specific priors to constrain the model parameters. This approach was successfully tested on two benchmark galaxies with very accurate, independent M_{BH} determinations: the massive elliptical galaxy M87 (D. A. Simon et al. 2024) and the spiral galaxy NGC 4258 (D. D. Nguyen et al. 2026), which has a morphology similar to M81. In both cases, the JAMs with these physically motivated priors recovered the known BH masses, validating the reliability of this method.

Following this validated approach, we restricted the inner anisotropy to be tangentially biased or isotropic ($0.5 < (\sigma_r/\sigma_\theta)_0 < 1$) and the outer anisotropy to be isotropic or mildly radially biased ($1 < (\sigma_r/\sigma_\theta)_\infty < 1.3$). The anisotropy transition radius was fixed at $r_a = 0''.55$, slightly larger than the SMBH's SOI ($r_{\mathrm{SOI}} \approx 0''.5$; see Section 5.1), to ensure the model can capture the expected transition from a tangentially biased inner region to a more isotropic outer region. Finally, we fixed the sharpness parameter to $\alpha = 2$ to reduce the dimensionality of the parameter space and minimize degeneracies.

4.5. Markov Chain Monte Carlo Fitting and Uncertainty Estimation

We ran the JAMs within a Markov Chain Monte Carlo (MCMC) framework to explore the full parameter space. Sampling was performed using the adaptive Metropolis algorithm (H. Haario et al. 2001), as implemented in the ADAMET[20] package (M. Cappellari et al. 2013). Each MCMC chain comprised 5×10^4 steps, with the first 20% of samples discarded as burn in. The remaining samples were used to construct posterior probability distributions. The most likely values for the model parameters were identified as those corresponding to the maximum likelihood, and uncertainties were estimated from the 1σ (16th–84th percentiles) and 3σ (0.14th–99.86th percentiles) confidence intervals.

Although our JAM dynamical modeling incorporates the formal kinematic measurement uncertainties, including an $\sim$15% uncertainty on the central bin kinematics to account for AGN contamination, the large number of high-precision NIRSpec kinematic data points introduces two challenges.

1. *Underestimated uncertainties*. The formal statistical errors on derived parameters can become unrealistically small due to the unmodelled systematic effects.
2. *Dominance of large-radius data*. The χ^2 statistic can be disproportionately influenced by the large number of data points at large radii. This risks biasing the $M_{\rm BH}$ measurement, which should be dictated primarily by the kinematics within the BH's SOI.

To mitigate the first issue, we adopt an error inflation scheme. We base our approach on the heuristic $\Delta\chi^2$-increase method of R. C. E. van den Bosch & G. van de Ven (2009), which, in a Bayesian framework, is equivalent to inflating the kinematic measurement errors by a factor of $(2N)^{1/4}$, where N is the number of data points (M. Mitzkus et al. 2017, Section 6.1). While this technique is now standard for Atacama Large Millimeter/submillimeter Array–based $M_{\rm BH}$ measurements (e.g., E. V. North et al. 2019; M. D. Smith et al. 2019, 2021; D. D. Nguyen et al. 2020), a uniform inflation across all radii does not resolve the second challenge.

Therefore, we apply the inflation selectively. We preserve the formal kinematic uncertainties for all data points inside the SOI ($r \leqslant r_{\rm SOI} \approx 0\farcs5$), where the SMBH's gravitational potential dominates. For the $N_{r>r_{\rm SOI}} = 620$ kinematic bins outside this radius, we inflate their associated errors by a factor of $(2N_{r>r_{\rm SOI}})^{1/4}$. This refined strategy ensures the $M_{\rm BH}$ determination is driven by the central kinematics while still accounting for potential systematic errors at larger radii. This selective approach has been successfully employed in previous dynamical studies using IFU data from Gemini/NIFS (D. A. Drehmer et al. 2015), Very Large Telescope (VLT)/MUSE (S. Thater et al. 2022, Section 4.3), and recently JWST/NIRSpec (D. D. Nguyen et al. 2026).

5. Results and Discussion

5.1. Dynamical Supermassive Black Hole Mass Constraints

We summarize in Table 4 the best-fit parameters and their 1σ uncertainties for the 12 conventional JAMs used to fit the NIRSpec G235H/F170LP $V_{\rm rms}$ data. Across all model assumptions, the inferred $M_{\rm BH}$ ranges from (4.51–5.14) $\times 10^7\ M_\odot$, and the M/L_J values span (1.69–2.02) ($M_\odot/L_\odot$). While both $M_{\rm BH}$ and M/L_J are relatively insensitive to the choice of PSF, they are more strongly affected by the assumed velocity-ellipsoid alignment. Specifically, the $\rm JAM_{cyl}$ models yield $M_{\rm BH}$ and M/L_J values that are $\approx$7% higher than those from the $\rm JAM_{sph}$ models.

Figure 10 shows the $V_{\rm rms}$ profiles for all 12 best-fitting JAMs (with their 1σ uncertainties), extracted along the major and minor axis of M81. These are directly compared to the observed $V_{\rm rms}$ profiles from the NIRSpec G235H/F170LP data, extracted in the same manner. Overall, all models provide a good match to both the data and to each other across the NIRSpec FOV, despite differences in the assumed M/L_J profiles and orbital anisotropy.

A systematic offset is observed between the models and the data in the innermost kinematic bins, which is likely attributable to uncertainties in the NIRSpec PSF modeling. To investigate this, we tested three synthetic PSFs from D. D. Nguyen et al. (2026) with different widths. The models using the broadest PSF (PSF3, $\rm FWHM^{tot}_{PSF} \approx 0\farcs2$), consistently underpredict the central $V_{\rm rms}$ by $\approx$20 km s^{-1} (right column of Figure 10). Conversely, models with the narrowest PSF (PSF1, $\rm FWHM^{tot}_{PSF} \approx 0\farcs08$) tend to overpredict the central $V_{\rm rms}$ by $\approx$15 km s^{-1} (left column). The models providing the best match to the data, including the innermost bins, are those using the intermediate PSF2 ($\rm FWHM^{tot}_{PSF} \approx 0\farcs15$; middle column). This preference for the $\approx 0\farcs15$ PSF is consistent with the findings for NGC 4258 in D. D. Nguyen et al. (2026), giving us confidence that our models are using a realistic representation of the instrumental resolution.

Notably, our derived $M_{\rm BH}$ value is 17% lower than that inferred from the VLT/GMOS IFU velocity dispersion and the K. Gültekin et al. (2009) $M_{\rm BH}$–σ relation, while it is 31.7% lower than the gas-based $M_{\rm BH}$ measurement from HST/STIS (N. Devereux et al. 2003) and 26.5% lower than the widely adopted value from J. Kormendy & L. C. Ho (2013). More specifically, the derived $M_{\rm BH}$ values are insensitive to the assumed alignment of the velocity ellipsoid but are sensitive to the adopted M/L_J profile in the nucleus of M81.

In contrast, the orbital anisotropy of the nuclear stellar motions in M81 is well constrained and does not depend on whether a constant or varying M/L_J is assumed. The best-fit $\rm JAM_{cyl}$ models indicate nearly isotropic kinematics, with $\sigma_z/\sigma_R \sim 1$ (i.e., $\beta_z \sim 0$). For the $\rm JAM_{sph}$ models, we adopt a fixed transition radius $r_a = 0\farcs55$ (see Section 4.4). The best-fit models indicate that the ratio of stellar velocity dispersions $(\sigma_r/\sigma_\theta)_0$ at the center varies from $\sim$0.55 to $\sim$1.0 depending on the adopted PSF model (i.e., $\beta_r < 0$) and suggesting a slightly tangential bias. Beyond r_a, the orbits transition to a radially biased structure with $(\sigma_r/\sigma_\theta)_\infty \sim 1.20$ (i.e., $\beta_r > 0$).

Additionally, to further assess the robustness of our JAM results against AGN contamination, we repeated the dynamical modeling after masking the two innermost bins in Figure 10, which both have stellar fraction $\gamma < 0.5$ (Figure 8), both are the most affected by AGN contamination ($\sim$15%), and probably the most influential in constraining $M_{\rm BH}$. We carried out this test across the same 12 JAM configurations presented in Figure 10, resulting in a total of 24 models when combined with the original set. We note that this pool of 24 models contains systematic uncertainties propagated from the kinematic measurements, including cases with AGN contamination and cases where the two innermost AGN-affected bins are completely excluded.

[20] v2.0.9: https://pypi.org/project/adamet/

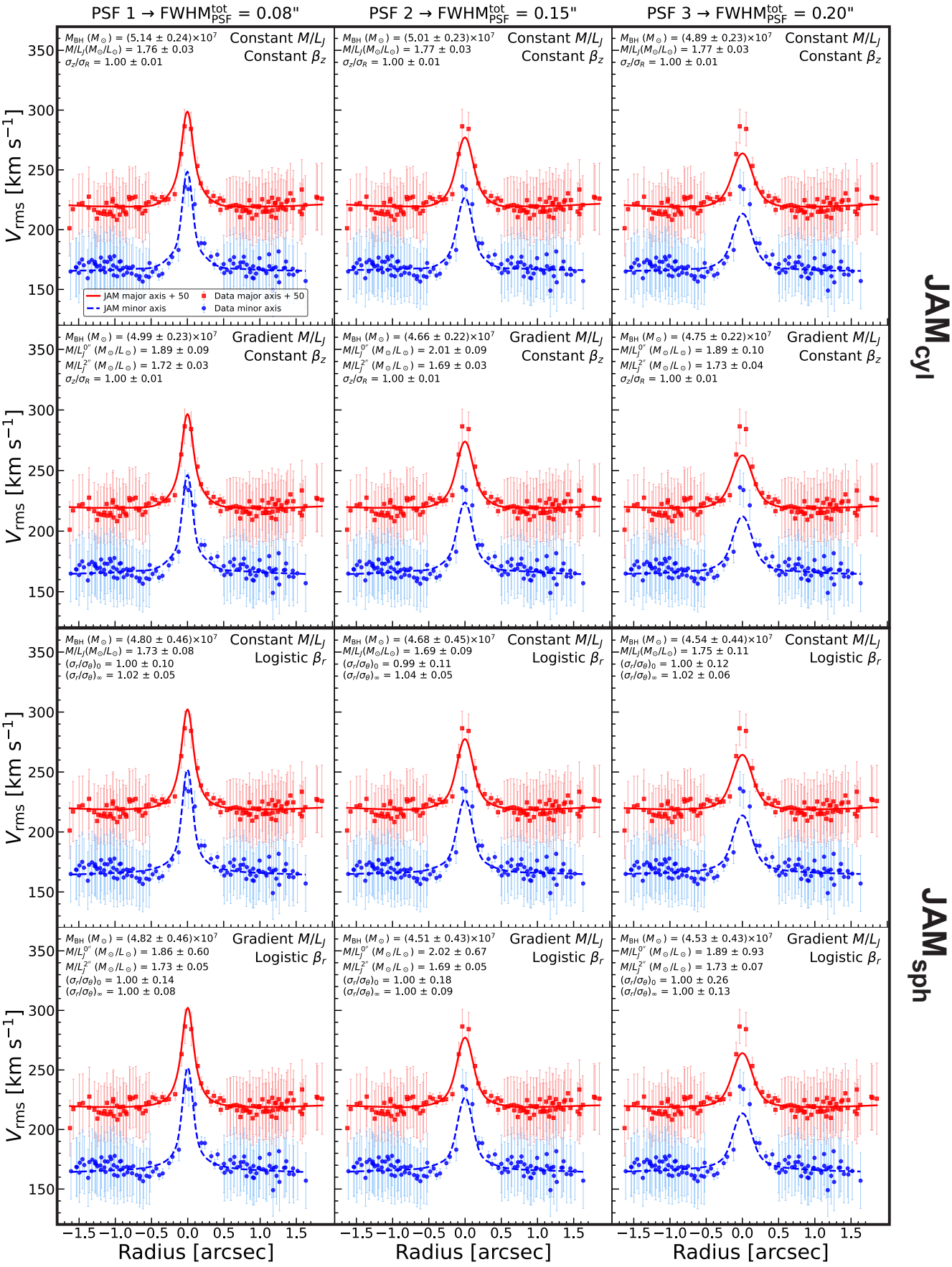

Figure 10. Stellar kinematics extracted from the NIRSpec G235H/F170LP data cube of M81 are shown as filled red (major axis + 50 km s^{-1}) and blue (minor axis) points, overlaid with best-fit JAMs assuming various combinations of M/L_J and orbital anisotropy. Each model includes its corresponding best-fit parameters and associated 1σ uncertainties in the legend.

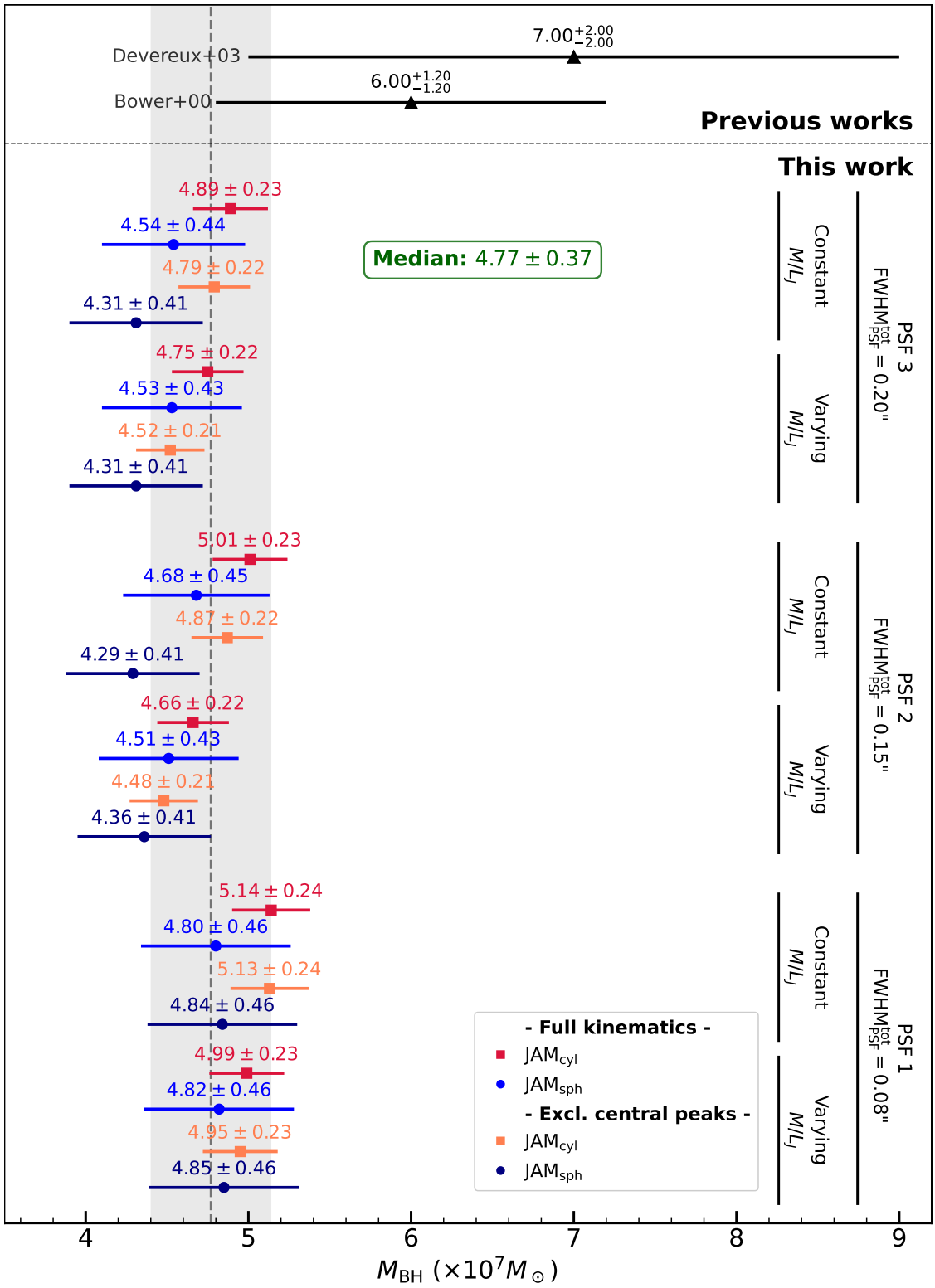

Figure 11. BH mass measurements for M81 derived from 12 standard JAMs and an additional 12 models that exclude the two innermost kinematic bins, which are strongly affected by AGN contamination, applied to the NIRSpec G235H/F170LP data cube. Individual measurements and their 1σ uncertainties reflect variations from the stellar-kinematic measurements, including those arising from AGN contamination in the central bins, the PSF, the orbital anisotropy, and the stellar M/L_J assumptions. The vertical dashed line marks the adopted M_{BH}, while the gray shaded region represents the total error budget, including both statistical and systematic uncertainties. For comparison, previous estimates from G. A. Bower et al. (2000) and N. Devereux et al. (2003) are shown; these earlier values relied on more restrictive stellar dynamical assumptions or disturbed ionized gas kinematics, respectively. Our present analysis provides the most robust measurement of M_{BH} in M81 to date.

Figure 11 shows our 24 M_{BH} measurements and their 1σ uncertainties, providing a presentation-ready summary of the most precise M_{BH} constraint for M81 based on the spatially resolved NIRSpec G235H/F170LP IFU stellar kinematics. Following the approach of D. D. Nguyen et al. (2026), we derive robust SMBH estimates from the 24

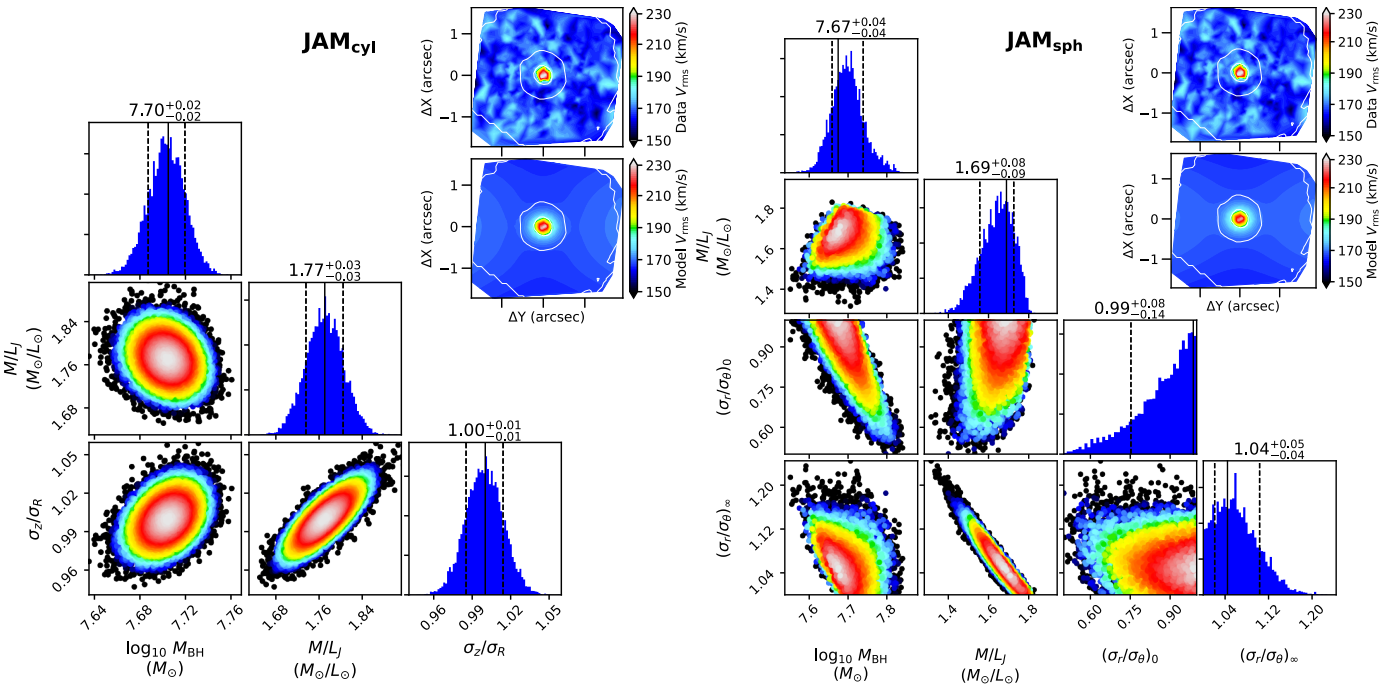

Figure 12. Left: posterior distributions for the JAM$_{cyl}$ model with constant M/L_J and anisotropy, obtained following the burn-in phase of the ADAMET MCMC optimization, are presented for the nuclear stellar kinematics of M81 using the NIRSpec G235H/F170LP data. The resulting triangle plot displays the 2D projected probability distributions of the model parameters (M_{BH}, M/L_J, and σ_z/σ_R), with 1D marginalized histograms shown along the diagonal. Solid vertical lines indicate the best-fit values, while dashed lines denote the 1σ uncertainties. Inset panels in the upper right compare the observed and model-predicted V_{rms} on a consistent velocity scale. The observed V_{rms} map was symmetrized under the assumption of axisymmetry using the SYMMETRIZE_VELFIELD routine from the PLOTBIN (v.3.1.7)[21] package. Both the symmetrized data and model prediction were visualized with PLOT_VELFIELD. The strong agreement across the NIRSpec FOV demonstrates the high fidelity of the model. Right: same as the left panel, but applied the JAM$_{sph}$ models with a logistic varying β_r profile and the model parameters (M_{BH}, M/L_J, $(\sigma_r/\sigma_\theta)_0$, and $(\sigma_r/\sigma_\theta)_\infty$).

conventional JAMs by adopting the medians and their 68% (1σ) statistic bootstrapping confidence intervals, yielding $M_{BH} = (4.77^{+0.05}_{-0.11}) \times 10^7\ M_\odot$.

The bootstrapped median M_{BH} derived from the 24 models differs by only 0.2% relative to the value produced from the 12 original models shown in Figure 10 and Table 4, while the associated statistical and systematic uncertainties remain essentially unchanged. We therefore conclude that our M_{BH} determination is robust against the most uncertain regions of the kinematic map.

To construct a comprehensive uncertainty budget, we combine in quadrature the medians of the formal systematic uncertainty and the statistical uncertainty. Following common practice in BH determination, the uncertainty due to the assumed distance is excluded, as M_{BH} scales linearly with distance and how this contributes to the uncertainty is treated separately. This yields a complete uncertainty budget on our M_{BH} determination of $M_{BH} = (4.77 \pm 0.37) \times 10^7\ M_\odot$.

Figure 12 shows example 2D posterior distributions for the JAM$_{cyl}$ model with constant anisotropy (left) and the JAM$_{sph}$ model with logistic anisotropy (Equation (2); right). Both models assume a constant M/L_J within the NIRSpec FOV and PSF2. Point colors indicate relative likelihood, with white corresponding to the maximum likelihood and the 1σ confidence level (CL) region, and black marking the 3σ CL. The accompanying 1D histograms along the diagonal are used to determine the best-fit values and 1σ uncertainties, which incorporate the propagation of stellar kinematics and statistical errors. The figure also demonstrates the close agreement between the observed V_{rms} and the predictions from the best-fit JAM$_{cyl}$ and JAM$_{sph}$ models at the upper right corner of each triangle, assuming the major axes are aligned horizontally, with relative errors less than 5% in each case.

In the best-fitting JAM$_{cyl}$ model, the remaining two parameters are well constrained, whereas in the best-fitting JAM$_{sph}$ model, only the M_{BH} and M/L_J parameters are well constrained. The other parameters of the logistic anisotropy are limited by their priors to enforce physically plausible stellar orbits around the SMBH and within the NIRSpec FOV.

Across all JAMs, there is no significant covariance between M_{BH} and M/L_J within the 3σ CLs, indicating that both parameters are well constrained. In the JAM$_{cyl}$ model, M_{BH} and M/L_J each show positive covariance with the orbital anisotropy parameter (σ_z/σ_R), whereas in the JAM$_{sph}$ model, these covariances are negative with respect to (σ_θ/σ_r). This contrast highlights the complexity of how variations in M_{BH} or M/L_J can compensate for changes in anisotropy during the fitting process.

Our stellar-based M_{BH} measurements, derived under both cylindrical and spherical velocity-ellipsoid assumptions, yield $r_{SOI} \approx 0\farcs5$ (or 9 pc), estimated using the method described in Section 1. These values are 5 times larger than the JWST spatial resolution, indicating that the M_{BH} determinations are robust and spatially well resolved. The dynamical influence of the SMBH is clearly detected within the central ≈80 spaxels in area.

5.2. The Mass–Anisotropy Degeneracy

A well-known characteristic of Jeans modeling is the mass–anisotropy degeneracy, where a given kinematic profile can be fit by different combinations of mass and orbital anisotropy.

[21] https://pypi.org/project/plotbin/

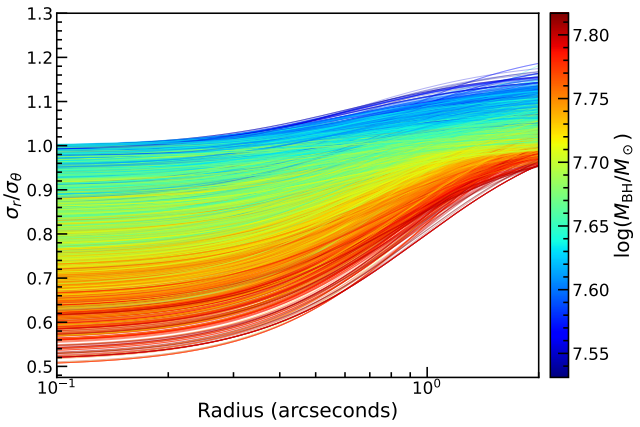

Figure 13. Plot of 10,000 anisotropy profiles randomly sampled from the MCMC chain of the JAM_{sph} model with logistic anisotropy Figure 12, color coded by their corresponding M_{BH} values. The profiles show clear evidence of a radially increasing anisotropy ratio and strongly exhibit the BH mass–anisotropy degeneracy like M87 (D. A. Simon et al. 2024) and NGC 4258 (D. D. Nguyen et al. 2026). The orbital anisotropy varies with BH mass: stars orbiting more massive BHs exhibit tangentially biased motions, whereas those around less massive BHs show radial anisotropy.

This effect is clearly illustrated in Figure 13, which shows 10,000 anisotropy profiles randomly drawn from the posterior distribution of our logistic JAM_{sph} model. The figure shows the expected covariance between M_{BH} and the anisotropy profile: higher M_{BH} values are required to fit the data when the stellar orbits are more tangentially biased, while lower M_{BH} values are consistent with more radial orbits. This behavior is not a flaw in our approach but an inherent property of stellar dynamics, and it has been observed in similar analyses of other galaxies like NGC 4258 (Figure 9 of D. D. Nguyen et al. 2026) and M87 (Figure 15 of D. A. Simon et al. 2024).

What is crucial for a reliable mass measurement is that this degeneracy is properly sampled and accounted for in the final uncertainty budget. Our Bayesian MCMC framework is designed to do precisely this. By exploring the full parameter space, the sampler covers all degenerate solutions consistent with the data and our physically motivated priors. The final posterior probability distribution for M_{BH} is marginalized over all other parameters, including the full range of allowed anisotropy profiles. Therefore, the reported CLs on our M_{BH} measurement robustly incorporate the uncertainty arising from the mass–anisotropy degeneracy.

5.3. Additional Uncertainty Budgets

5.3.1. Distances

Unlike most galaxies, the distance to M81 is exceptionally well determined. As stated in Section 1, we adopt a distance of $D = 3.63 \pm 0.14$ Mpc, which is the mean of five high-quality determinations based on the Cepheid and TRGB methods. This precision is corroborated by the NASA/IPAC NED, which lists 99 distance determinations, yielding a formal average of 3.675 ± 0.049 Mpc.

Although the distance is robust, its uncertainty remains a dominant source of systematic error in our final BH mass. Since M_{BH} scales linearly with distance ($M_{BH} \propto D$), the ± 0.049 Mpc uncertainty from the NED average and ± 0.14 Mpc uncertainty from our adopted distance propagate to systematic uncertainties of $\pm 1.3\%$ and $\pm 2.9\%$ in our M_{BH} measurement, respectively. This is comparable to the formal statistical errors from our dynamical models and thus represents a key component of the total error budget.

5.3.2. Active-galactic-nucleus-contaminated Stellar-mass Model

We evaluated the impact of the HST AGN contamination on the M_{BH} and M/L_J measurements by replacing our best-fitting, combined, and AGN-free MGE model (Table 3) by the similar best-fitting and combined but AGN-contaminated MGE model (Section 3.5), which is shown in a black line in the right panel of Figure 8. The enclosed luminosity difference within $1''$ between the AGN-free and AGN-contaminated MGE models is $8.5 \times 10^6\ L_\odot$. Adopting the constant M/L_J from either the JAM_{cyl} or JAM_{sph} models, this corresponds to a stellar-mass difference of $(1.4–1.5) \times 10^7\ M_\odot$, introducing an ~11%–20% uncertainty in the M_{BH} estimates under the fixed M/L_J and anisotropy values as presented in Table 4.

More realistic tests allowed both M_{BH} and M/L_J to vary in the JAM_{cyl} and JAM_{sph} models using the AGN-contaminated MGE model. The best-fitting JAM_{cyl} model with constant M/L_J yields $M_{BH} = (4.26 \pm 0.21) \times 10^7\ M_\odot$ and $M/L_J = 1.79 \pm 0.03\ (M_\odot/L_\odot)$, while the corresponding JAM_{sph} model gives $M_{BH} = (3.81 \pm 0.36) \times 10^7\ M_\odot$ and $M/L_J = 1.49 \pm 0.09\ (M_\odot/L_\odot)$. All other parameters differ by less than 8% from the values in Table 4 and are discussed in Section 5.1. The close agreement with the results obtained using the AGN-free MGE model indicates that AGN light in the central region, adding to the stellar mass, introduces uncertainty in the M_{BH} estimates.

5.3.3. Alternative Stellar-kinematic Measurements

We additionally derived the stellar kinematics of M81 from the NIRSpec G235H/F170LP data using an alternative setup based on the higher-resolution PHOENIX synthetic stellar library (Section 2.4; T.-O. Husser et al. 2013) and adopting `moments = 2` in PPXF. The resulting kinematics is consistent with our fiducial measurements, which employ the XSL library with `moments = 2`, to within 3%. We evaluated the impact of these alternative kinematic measurements on the inferred M_{BH} and M/L_J and find that the resulting systematic differences are negligible.

5.4. M_{BH}–Galaxy Scaling Relations

We examine the location of the central SMBH in M81 relative to the established M_{BH}–σ, M_{BH}–$M_{\star,sph}$, and M_{BH}–$M_{\star,gal}$ scaling relations. We adopt a stellar velocity dispersion of $\sigma_e = (165 \pm 4)$ km s^{-1}, measured outside the SMBH's SOI, along with stellar-mass estimates of $\log(M_{\star,sph}) = (10.16 \pm 0.11)\ M_\odot$ for the spheroidal component (B. L. Davis et al. 2019) and $\log(M_{\star,gal}) = (10.65 \pm 0.08)\ M_\odot$ for the total galaxy (B. L. Davis et al. 2018). Using these values, we placed M81 on the M_{BH}–σ relations from J. Kormendy & L. C. Ho (2013) and R. C. E. van den Bosch (2016; see Figure 14), as well as on the M_{BH}–$M_{\star,sph}$ and M_{BH}–$M_{\star,gal}$ relations from J. Kormendy & L. C. Ho (2013) and A. W. Graham & N. Sahu (2023). The relations presented by J. Kormendy & L. C. Ho (2013) and R. C. E. van den Bosch (2016) combine spiral, lenticular, and elliptical galaxies, whereas A. W. Graham & N. Sahu (2023) provide morphology-dependent fits; for the latter, we adopt the spiral-galaxy relations. The BH masses used to define these scaling relations are predominantly derived from dynamical measurements based on gas, maser, and stellar kinematics; in the case of the M_{BH}–σ relation, they are

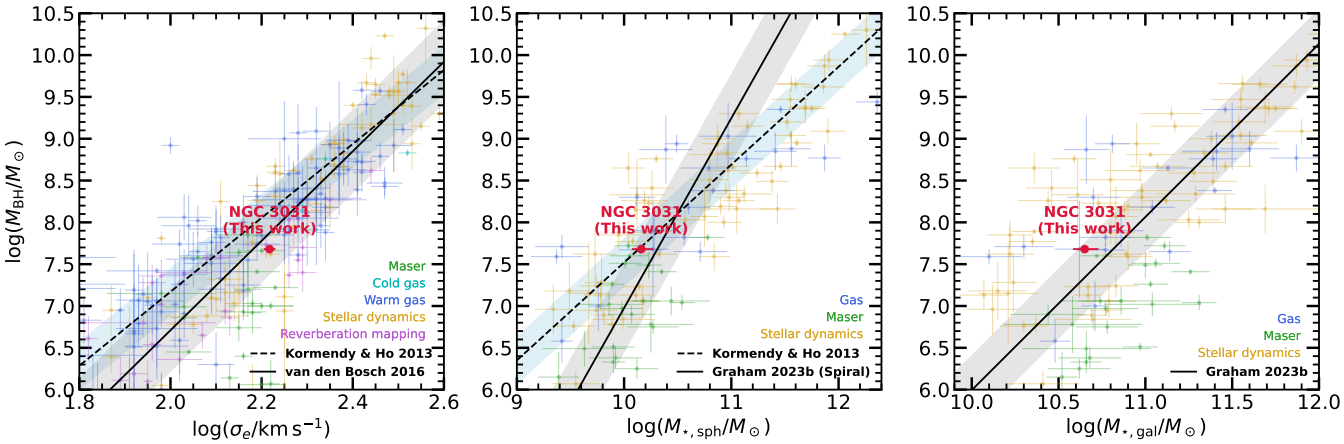

Figure 14. Location of M81 with respect to the $M_{\rm BH}$–σ (left), $M_{\rm BH}$–$M_{\star,\rm sph}$ (middle), $M_{\rm BH}$–$M_{\star,\rm gal}$ (right) scaling relations. Our new measurements are consistent within 1σ with the $M_{\rm BH}$–σ scaling relations for spiral galaxies.

additionally included BH masses obtained via reverberation mapping.

Our measured $M_{\rm BH}$ for M81 is consistent within 1σ of the R. C. E. van den Bosch (2016) $M_{\rm BH}$–σ relation and within 2σ of the J. Kormendy & L. C. Ho (2013) relation. Similarly, M81 lies within 1σ of both the J. Kormendy & L. C. Ho (2013) and A. W. Graham & N. Sahu (2023) $M_{\rm BH}$–$M_{\star,\rm sph}$ relations, as well as the A. W. Graham & N. Sahu (2023) $M_{\rm BH}$–$M_{\star,\rm gal}$ relation.

6. Conclusions

We have presented the first robust stellar-dynamics measurement of the SMBH mass in the nearby spiral galaxy M81. Previous determinations were unreliable, being based on disturbed gas kinematics or preliminary stellar-dynamics models. Our analysis leverages the power of JWST/NIRSpec IFU observations, which provide high-resolution 2D stellar kinematics in the NIR, allowing us to penetrate the dusty nucleus and cleanly separate stellar light from the AGN continuum. Our main results are as follows.

1. The NIRSpec data clearly resolve the BH's SOI. We measured a sharp rise in the stellar velocity dispersion from 165 km s^{-1} at large radii to a central peak of 233 $\pm$ 15 km s^{-1}, providing unambiguous kinematic evidence for a central dark mass.
2. We performed a comprehensive dynamical analysis using an ensemble of 24 JAMs to systematically account for uncertainties in the instrumental PSF, stellar *M/L* ratio, and orbital anisotropy. This robust approach yields a BH mass of $M_{\rm BH} = (4.77 \pm 0.37) \times 10^7\ M_\odot$.
3. Our models confirm the expected mass–anisotropy degeneracy, where more tangentially biased orbits require a more massive BH. Our Bayesian framework fully explores this degeneracy, and its effect is incorporated into our final quoted uncertainties.
4. This new, reliable mass measurement for M81 resolves a long-standing uncertainty. It provides a crucial anchor point for SMBH–galaxy scaling relations, particularly for spiral galaxies, where it is consistent with the established $M_{\rm BH}$–σ and $M_{\rm BH}$–$M_{\star,\rm gal}$ relations.

Acknowledgments

The authors would like to thank the anonymous referee for their careful reading and useful comments, which helped to improve this paper greatly. N.T. would like to acknowledge partial support from UKRI grant ST/X002322/1 for UK ELT Instrument Development at Oxford. M.P. acknowledges support through the grants PID2021-127718NB-I00 and RYC2023-044853-I, funded by the Spanish Ministry of Science and Innovation/State Agency of Research MCIN/AEI/10.13039/501100011033 and El Fondo Social Europeo Plus FSE+. M.P.S. acknowledges support under grants RYC2021-033094-I, CNS2023-145506, and PID2023-146667NB-I00 funded by MCIN/AEI/10.13039/501100011033 and the European Union NextGenerationEU/PRTR.

This research is based on observations made with the NASA/ESA Hubble Space Telescope obtained from the Space Telescope Science Institute, which is operated by the Association of Universities for Research in Astronomy, Inc., under NASA contract NAS 5–26555. This work is based [in part] on observations made with the NASA/ESA/CSA James Webb Space Telescope. The data were obtained from the Mikulski Archive for Space Telescopes at the Space Telescope Science Institute, which is operated by the Association of Universities for Research in Astronomy, Inc., under NASA contract NAS 5-03127 for JWST. These observations are associated with program #02016.

Some/all of the data presented in this article were obtained from the Mikulski Archive for Space Telescopes (MAST) at the Space Telescope Science Institute. The specific observations analyzed can be accessed via DOI: 10.17909/cbpe-ft90.

Facilities: JWST/NIRSpec, HST/WFC3, FLWO:2MASS.

Software: `Python 3.12` (G. Van Rossum & F. L. Drake 2009), `Matplotlib 3.6` (J. D. Hunter 2007), `NumPy 1.22` (C. R. Harris et al. 2020), `SciPy 1.3` (P. Virtanen et al. 2020), `photutils 0.7` (L. Bradley et al. 2024), `AstroPy 5.1` (Astropy Collaboration et al. 2022), ADAMET 2.0 (M. Cappellari et al. 2013), JAMPY 7.2 (M. Cappellari 2020), PPXF 8.2 (M. Cappellari 2023), `vorbin 3.1` (M. Cappellari & Y. Copin 2003), and MGEFIT 5.0 (M. Cappellari 2002).

ORCID iDs

Dieu D. Nguyen https://orcid.org/0000-0002-5678-1008
Tuan N. Le https://orcid.org/0009-0009-0015-1208

Michele Cappellari https://orcid.org/0000-0002-1283-8420
Hai N. Ngo https://orcid.org/0009-0006-5852-4538
Tinh Q. T. Le https://orcid.org/0009-0004-3689-8577
Tien H. T. Ho https://orcid.org/0009-0005-8845-9725
Long Q. T. Nguyen https://orcid.org/0009-0006-4602-1968
Elena Gallo https://orcid.org/0000-0001-5802-6041
Fan Zou https://orcid.org/0000-0002-4436-6923
Michele Perna https://orcid.org/0000-0002-0362-5941
Niranjan Thatte https://orcid.org/0000-0002-6694-5184
Miguel Pereira-Santaella https://orcid.org/0000-0002-4005-9619

References

Ahn, C. P., Seth, A. C., Cappellari, M., et al. 2018, ApJ, 858, 102
Astropy Collaboration, Price-Whelan, A. M., Lim, P. L., et al. 2022, ApJ, 935, 167
Barth, A. J., Sarzi, M., Rix, H. W., et al. 2001, ApJ, 555, 685
Batcheldor, D., Robinson, A., Axon, D. J., Perlman, E. S., & Merritt, D. 2010, ApJL, 717, L6
Bender, R., Saglia, R. P., & Gerhard, O. E. 1994, MNRAS, 269, 785
Bentz, M. C. 2025, RNAAS, 9, 128
Binney, J., & Mamon, G. A. 1982, MNRAS, 200, 361
Bower, G. A., Wilson, A. S., Heckman, T. M., et al. 2000, AAS, 197, 92.03
Bradley, L., Sipőcz, B., Robitaille, T., et al. 2024, astropy/photutils: v2.0.2,
Bushouse, H., Eisenhamer, J., Dencheva, N., et al. 2024, JWST Calibration Pipeline, v1.14.0,
Cappellari, M. 2002, MNRAS, 333, 400
Cappellari, M. 2008, MNRAS, 390, 71
Cappellari, M. 2017, MNRAS, 466, 798
Cappellari, M. 2020, MNRAS, 494, 4819
Cappellari, M. 2023, MNRAS, 526, 3273
Cappellari, M. 2026, in Encyclopedia of Astrophysics, ed. I. Mandel, Vol. 4 (Elsevier), 122
Cappellari, M., & Copin, Y. 2003, MNRAS, 342, 345
Cappellari, M., & Emsellem, E. 2004, PASP, 116, 138
Cappellari, M., Neumayer, N., Reunanen, J., et al. 2009, MNRAS, 394, 660
Cappellari, M., Scott, N., Alatalo, K., et al. 2013, MNRAS, 432, 1709
Chu, Q., Yu, S., & Lu, Y. 2022, MNRAS, 509, 1557
Dalcanton, J. J., Williams, B. F., Seth, A. C., et al. 2009, ApJS, 183, 67
Davis, B. L., Graham, A. W., & Cameron, E. 2018, ApJ, 869, 113
Davis, B. L., Graham, A. W., & Cameron, E. 2019, ApJ, 873, 85
Davis, T. A., Bureau, M., Cappellari, M., Sarzi, M., & Blitz, L. 2013, Natur, 494, 328
Davis, T. A., Nguyen, D. D., Seth, A. C., et al. 2020, MNRAS, 496, 4061
D'Eugenio, F., Juodžbalis, I., Ji, X., et al. 2026, MNRAS, 545, staf2117
D'Eugenio, F., Pérez-González, P., Maiolino, R., et al. 2024, NatAs, 8, 1443
Devereux, N., Ford, H., Tsvetanov, Z., & Jacoby, G. 2003, AJ, 125, 1226
Drehmer, D. A., Storchi-Bergmann, T., Ferrari, F., Cappellari, M., & Riffel, R. A. 2015, MNRAS, 450, 128
Durrell, P. R., Sarajedini, A., & Chandar, R. 2010, ApJ, 718, 1118
Emsellem, E., Monnet, G., & Bacon, R. 1994, A&A, 285, 723
Eracleous, M., Hwang, J. A., & Flohic, H. M. L. G. 2010, ApJS, 187, 135
Ferrarese, L., Mould, J. R., Kennicutt, R. C., Jr., et al. 2000, ApJ, 529, 745
Freedman, W. L., Hughes, S. M., Madore, B. F., et al. 1994, ApJ, 427, 628
Gebhardt, K., Richstone, D., Tremaine, S., et al. 2003, ApJ, 583, 92
Graham, A. W., & Sahu, N. 2023, MNRAS, 520, 1975
Gültekin, K., Richstone, D. O., Gebhardt, K., et al. 2009, ApJ, 698, 198
Haario, H., Saksman, E., & Tamminen, J. 2001, Bernoulli, 7, 223
Harris, C. R., Millman, K. J., van der Walt, S. J., et al. 2020, Natur, 585, 357
Hunter, J. D. 2007, CSE, 9, 90
Husser, T.-O., Wende-von Berg, S., Dreizler, S., et al. 2013, A&A, 553, A6
Jarrett, T. H., Chester, T., Cutri, R., Schneider, S. E., & Huchra, J. P. 2003, AJ, 125, 525
Kormendy, J., & Bender, R. 1999, ApJ, 522, 772
Kormendy, J., & Ho, L. C. 2013, ARA&A, 51, 511
Krajnović, D., Cappellari, M., de Zeeuw, P. T., & Copin, Y. 2006, MNRAS, 366, 787
Krajnović, D., Cappellari, M., McDermid, R. M., et al. 2018, MNRAS, 477, 3030
Krist, J. 1995, ASPC, 77, 349
Krist, J. E., Hook, R. N., & Stoehr, F. 2011, SPIE, 8127, 81270J
Lauer, T. R., Faber, S. M., Ajhar, E. A., Grillmair, C. J., & Scowen, P. A. 1998, AJ, 116, 2263
Lauer, T. R., Faber, S. M., Gebhardt, K., et al. 2005, AJ, 129, 2138
Law, D. R., E. Morrison, J., Argyriou, I., et al. 2023, AJ, 166, 45
Lena, D., Robinson, A., Marconi, A., et al. 2014, ApJ, 795, 146
Marconi, A., Schreier, E. J., Koekemoer, A., et al. 2000, ApJ, 528, 276
McCommas, L. P., Macri, L. M., Rejkuba, M., et al. 2009, ApJS, 185, 1
McConnell, N. J., & Ma, C.-P. 2013, ApJ, 764, 184
Milosavljević, M., & Merritt, D. 2001, ApJ, 563, 34
Mitzkus, M., Cappellari, M., & Walcher, C. J. 2017, MNRAS, 464, 4789
Müller-Sánchez, F., Comerford, J., Stern, D., & Harrison, F. A. 2016, ApJ, 830, 50
Neumayer, N., Cappellari, M., Reunanen, J., et al. 2007, ApJ, 671, 1329
Ngo, H. N., Nguyen, D. D., Le, T. T. Q., et al. 2025, Univ, 11, 360
Ngo, H. N., Nguyen, D. D., Le, T. Q. T., et al. 2025b, ApJ, 992, 211
Ngo, H. N., Nguyen, D. D., Nguyen, T. N., Dang, T. H., & Ho, T. H. T. 2025a, arXiv, arXiv:2509.03364
Nguyen, D. D. 2017, arXiv, arXiv:1712.02470
Nguyen, D. D. 2019, ALMA2019: Science Results and Cross-Facility Synergies, v1 Zenodo, doi:10.5281/zenodo.3585410
Nguyen, D. D., Bureau, M., Thater, S., et al. 2022, MNRAS, 509, 2920
Nguyen, D. D., Cappellari, M., Ngo, H. N., et al. 2025a, AJ, 170, 124
Nguyen, D. D., Cappellari, M., & Pereira-Santaella, M. 2023, MNRAS, 526, 3548
Nguyen, D. D., den Brok, M., Seth, A. C., et al. 2020, ApJ, 892, 68
Nguyen, D. D., Izumi, T., Thater, S., et al. 2021, MNRAS, 504, 4123
Nguyen, D. D., Ngo, H. N., Cappellari, M., et al. 2026, ApJ, 999, 97
Nguyen, D. D., Ngo, H. N., Le, T. Q. T., et al. 2025b, A&A, 698, L9
Nguyen, D. D., Seth, A. C., den Brok, M., et al. 2017, ApJ, 836, 237
Nguyen, D. D., Seth, A. C., Neumayer, N., et al. 2018, ApJ, 858, 118
Nguyen, D. D., Seth, A. C., Neumayer, N., et al. 2019, ApJ, 872, 104
Nguyen, D. D., Seth, A. C., Reines, A. E., et al. 2014, ApJ, 794, 34
North, E. V., Davis, T. A., Bureau, M., et al. 2019, MNRAS, 490, 319
Onishi, K., Iguchi, S., Davis, T. A., et al. 2017, MNRAS, 468, 4663
Paturel, G., Petit, C., Prugniel, P., et al. 2003, A&A, 412, 45
Perna, M., Arribas, S., Marshall, M., et al. 2023, A&A, 679, A89
Perrin, M., Long, J., Osborne, S., et al. 2025, STPSF, v2.1.0,
Rantala, A., Rawlings, A., Naab, T., Thomas, J., & Johansson, P. H. 2024, MNRAS, 535, 1202
Rizzi, L., Tully, R. B., Makarov, D., et al. 2007, PASP, 661, 815
Saglia, R. P., Opitsch, M., Erwin, P., et al. 2016, ApJ, 818, 47
Sasseville, G., Hlavacek-Larrondo, J., Berek, S. C., et al. 2024, ApJ, 978, 48
Schlafly, E. F., & Finkbeiner, D. P. 2011, ApJ, 737, 103
Schnorr Müller, A., Storchi-Bergmann, T., Riffel, R. A., et al. 2011, MNRAS, 413, 149
Shapiro, K. L., Cappellari, M., de Zeeuw, T., et al. 2006, MNRAS, 370, 559
Shi, F., Li, Z., Yuan, F., & Zhu, B. 2021, NatAs, 5, 928
Silge, J. D., & Gebhardt, K. 2003, AJ, 125, 2809
Simon, D. A., Cappellari, M., & Hartke, J. 2024, MNRAS, 527, 2341
Smith, M. D., Bureau, M., Davis, T. A., et al. 2019, MNRAS, 485, 4359
Smith, M. D., Bureau, M., Davis, T. A., et al. 2021, MNRAS, 503, 5984
Tahmasebzadeh, B., Taylor, M. A., Valluri, M., et al. 2025, ApJL, 989, L42
Thater, S. 2019, ALMA2019: Science Results and Cross-Facility Synergies, v1 Zenodo, doi:10.5281/zenodo.3585459
Thater, S., Krajnović, D., Cappellari, M., et al. 2019, A&A, 625, A62
Thater, S., Krajnović, D., Weilbacher, P. M., et al. 2022, MNRAS, 509, 5416
Thater, S., Lyubenova, M., Fahrion, K., et al. 2023, A&A, 675, A18
Thatte, D., Dahlen, T., Barker, E., de Jong, R., & Koekemoer, A. 2009, NICMOS Data Handbook, Version 8.0 (Space Telescope Science Institute)
Thatte, N. A., Melotte, D., Neichel, B., et al. 2024, SPIE, 13096, 1309614
Tikhonov, N. A., & Galazutdinova, O. A. 2005, AstL, 31, 228
van den Bosch, R. C. E. 2016, ApJ, 831, 134
van den Bosch, R. C. E., & van de Ven, G. 2009, MNRAS, 398, 1117
van der Marel, R. P. 1994, MNRAS, 270, 271
van der Marel, R. P., & Franx, M. 1993, ApJ, 407, 525
Van Rossum, G., & Drake, F. L. 2009, Python 3 Reference Manual (CreateSpace)
Verolme, E. K., Cappellari, M., Copin, Y., et al. 2002, MNRAS, 335, 517
Verro, K., Trager, S. C., Peletier, R. F., et al. 2022, A&A, 660, A34
Virtanen, P., Gommers, R., Oliphant, T. E., et al. 2020, NatMe, 17, 261
Voggel, K. T., Seth, A. C., Neumayer, N., et al. 2018, ApJ, 858, 20
Walsh, J. L., van den Bosch, R. C. E., Gebhardt, K., et al. 2016, ApJ, 817, 2
Willmer, C. N. A. 2018, ApJS, 236, 47